

---

This work has been accepted to Journal of Climate. The AMS does not guarantee that the copy provided here is an accurate copy of the final published work.

---

1 **A data assimilation approach to last millennium temperature field**  
2 **reconstruction using a limited high-sensitivity proxy network**

3 Jonathan M. King\*

4 *Department of Geosciences and Laboratory of Tree-Ring Research, University of Arizona,*  
5 *Tucson, Arizona*

6 Kevin J. Anchukaitis

7 *School of Geography, Development, and Environment and Laboratory of Tree-Ring Research,*  
8 *University of Arizona, Tucson, Arizona*

9 Jessica E. Tierney

10 *Department of Geosciences, University of Arizona, Tucson, Arizona*

11 Gregory J. Hakim

12 *Department of Atmospheric Sciences, University of Washington, Seattle, Washington*

13 Julien Emile-Geay and Feng Zhu

14 *Department of Earth Sciences, University of Southern California, Los Angeles, California*

15 Rob Wilson

16 *School of Earth and Environmental Sciences, University of St Andrews, St Andrews, UK*

17 \*Corresponding author: Jonathan King, jonking93@email.arizona.edu

## ABSTRACT

18 We use the Northern Hemisphere Tree-Ring Network Development (NTREND) tree-ring database  
19 to examine the effects of using a small, highly-sensitive proxy network for paleotemperature data  
20 assimilation over the last millennium. We first evaluate our methods using pseudo-proxy experi-  
21 ments. These indicate that spatial assimilations using this network are skillful in the extratropical  
22 Northern Hemisphere and improve on previous NTREND reconstructions based on Point-by-Point  
23 regression. We also find our method is sensitive to climate model biases when the number of  
24 sites becomes small. Based on these experiments, we then assimilate the real NTREND network.  
25 To quantify model prior uncertainty, we produce 10 separate reconstructions, each assimilating a  
26 different climate model. These reconstructions are most dissimilar prior to 1100 CE, when the  
27 network becomes sparse, but show greater consistency as the network grows. Temporal variabil-  
28 ity is also underestimated before 1100 CE. Our assimilation method produces spatial uncertainty  
29 estimates and these identify treeline North America and eastern Siberia as regions that would  
30 most benefit from development of new millennial-length temperature-sensitive tree-ring records.  
31 We compare our multi-model mean reconstruction to five existing paleo-temperature products to  
32 examine the range of reconstructed responses to radiative forcing. We find substantial differences  
33 in the spatial patterns and magnitudes of reconstructed responses to volcanic eruptions and in  
34 the transition between the Medieval epoch and Little Ice Age. These extant uncertainties call for  
35 the development of a paleoclimate reconstruction intercomparison framework for systematically  
36 examining the consequences of proxy network composition and reconstruction methodology and  
37 for continued expansion of tree-ring proxy networks.

## 38 **1. Introduction**

39 Past variations in surface temperatures can be used to investigate a number of key characteristics  
40 of the Earth's climate system, including the response to radiative forcing, the regional effects of  
41 such forcings, and the role of internal modes of coupled ocean-atmosphere variability (Hegerl et al.  
42 1997; Stott and Tett 1998; Delworth and Mann 2000; Meehl et al. 2004; Lean and Rind 2008; Stott  
43 and Jones 2009; Stott et al. 2010; Solomon et al. 2011; Phipps et al. 2013; Hegerl and Stott 2014;  
44 Kaufman 2014; Guillet et al. 2017; Neukom et al. 2019; Zhu et al. 2020). Paleoclimate temperature  
45 reconstructions using natural archives like tree-rings are particularly useful because they extend  
46 the short instrumental record to centennial and longer timescales. These provide an opportunity  
47 to characterize the patterns and magnitude of forced climate response and internal variability  
48 (Hegerl et al. 2003, 2007; Schurer et al. 2013; Masson-Delmotte et al. 2013). Climate field  
49 reconstructions (CFRs) can additionally capture the spatial fingerprints of large-scale temperature  
50 anomalies caused by radiative forcing and ocean-atmosphere dynamics (Mann et al. 1998; Evans  
51 et al. 2001; Seager et al. 2007; Cook et al. 2010a,b; Phipps et al. 2013; Anchukaitis and McKay  
52 2015; Goosse 2017). CFRs have been developed using a number of methods (Tingley et al.  
53 2012; Smerdon and Pollack 2016) including point-by-point methods (Cook et al. 1999, 2010a,b;  
54 Anchukaitis et al. 2017), variants of regularized expectation maximization (RegEM; Schneider  
55 2001; Rutherford et al. 2003; Mann et al. 2009; Smerdon et al. 2011; Guillot et al. 2015), and  
56 reduced space approaches (Fritts 1991; Cook et al. 1994; Mann et al. 1998; Evans et al. 2002; Gill  
57 et al. 2016).

58 Recently, data assimilation (DA) has emerged as a promising CFR technique (e.g. Widmann  
59 et al. 2010; Bhend et al. 2012; Goosse et al. 2012; Steiger et al. 2014; Hakim et al. 2016; Matsikaris  
60 et al. 2015; Okazaki and Yoshimura 2017; Steiger et al. 2018; Franke et al. 2020). Assimilation

61 methods integrate the climate signals recorded in paleoclimate proxies with dynamical constraints  
62 provided by climate models to produce spatially continuous climate field reconstructions and  
63 associated uncertainty estimates. There are several existing paleoclimate DA paradigms, including  
64 pattern nudging / forcing singular vectors (Van der Schrier and Barkmeijer 2005), particle filters  
65 (Goosse et al. 2012; Dubinkina and Goosse 2013; Matsikaris et al. 2015), and ensemble Kalman  
66 filters (Bhend et al. 2012; Steiger et al. 2014; Hakim et al. 2016; Dee et al. 2016; Perkins and  
67 Hakim 2017; Steiger et al. 2018; Tardif et al. 2019; Franke et al. 2020). Here, we focus on the  
68 ensemble Kalman filter (EnKF) approach (Steiger et al. 2014; Hakim et al. 2016), which has been  
69 shown to perform well compared to other DA methods in a paleoclimate context (Liu et al. 2017).  
70 EnKF methods update an ensemble of climate states to more closely match paleoclimate proxy  
71 records. These climate states are produced using one of two approaches: the “online” method, in  
72 which the ensemble is generated by a set of transient model simulations that propagate updates  
73 forward through time (e.g. Perkins and Hakim 2017); and the “offline” (or “no-cycling”) method  
74 (Oke et al. 2002; Evensen 2003), in which ensembles are constructed from pre-existing climate  
75 model output (e.g. Bhend et al. 2012; Annan and Hargreaves 2012; Steiger et al. 2014; Hakim  
76 et al. 2016; Valler et al. 2019; Tardif et al. 2019; Franke et al. 2020). We focus here on the offline  
77 approach, which has been shown to perform favorably to online methods in paleoclimate contexts  
78 with reduced computational costs (Matsikaris et al. 2015; Acevedo et al. 2017). A key requirement  
79 of EnKF methods is the ability to estimate equivalent proxy values from climate model output. This  
80 is achieved through the use of forward models that translate climate state variables, like surface  
81 temperature, into proxy values, like tree-ring width (TRW) or maximum latewood density (MXD).  
82 These forward models can range in complexity from a simple linear relationship to more detailed  
83 Proxy Systems Models (PSMs) incorporating the physical processes that transform climate signals

84 to proxy records (Evans et al. 2013). The use of forward models helps separate data and process  
85 level models in the data assimilation framework (Goosse 2016).

86 An important decision in any assimilation is the selection of the proxy network. Ultimately,  
87 this choice must balance spatiotemporal coverage with sensitivity to the reconstructed field and  
88 associated proxy uncertainties (Esper et al. 2005; Frank et al. 2010; Wang et al. 2015; Wilson  
89 et al. 2016; Anchukaitis et al. 2017; Esper et al. 2018; Franke et al. 2020; Cort et al. 2021).  
90 In general, large networks maximize coverage, but their size often results from the inclusion of  
91 proxy records with comparatively weak, complex, seasonally varying, or multivariate sensitivity to  
92 reconstructed variables. By contrast, smaller curated networks consisting of well-understood and  
93 strongly-sensitive proxies provide a higher ratio of signal to noise at the cost of reduced coverage  
94 (Frank et al. 2010). An additional consideration concerns the implementation of forward models:  
95 highly sensitive networks with a known climate response and seasonal window facilitate physically  
96 realistic forward models, potentially improving assimilation skill. Given the complexity of these  
97 trade-offs, network selection is not necessarily intuitive. Noisy proxies that covary poorly with  
98 climate fields are down-weighted by the Kalman filter algorithm; if this down-weighting renders  
99 the effects of climate-insensitive proxies negligible on a reconstruction, then a large network  
100 incorporating many proxies might appear preferable. However, work by Franke et al. (2020)  
101 indicates that EnKF temperature reconstructions using large proxy networks do not correlate with  
102 target temperatures as well as reconstructions produced using smaller, more sensitive networks.  
103 This result is supported by Tardif et al. (2019), who found that additional screening of proxy records  
104 for temperature sensitivity in an assimilation framework improved their ability to reconstruct salient  
105 pre-industrial climate features, such as cooling during the Little Ice Age. The importance of proxy  
106 sensitivity is further highlighted by Steiger and Smerdon (2017) who note that skillful hydroclimate  
107 DA requires proxies sensitive to the target reconstruction field.

108 Curated temperature sensitive proxy networks for data assimilation include the PAGES2k  
109 (PAGES2k Consortium 2013, 2017) and NTREND networks (Wilson et al. 2016; Anchukaitis  
110 et al. 2017). The PAGES2k network has been commonly used in paleo-DA applications (Hakim  
111 et al. 2016; Dee et al. 2016; Okazaki and Yoshimura 2017; Perkins and Hakim 2017; Tardif et al.  
112 2019; Neukom et al. 2019) and consists of proxy records identified as temperature-sensitive and  
113 meeting minimum temporal coverage and age model precision criteria during the Common Era  
114 (PAGES2k Consortium 2017). DA reconstructions using this network may implement additional  
115 proxy screening but usually incorporate several hundred proxy records. The NTREND network  
116 has stricter requirements for inclusion: it consists of 54 published tree-ring chronologies selected  
117 by dendroclimatologists for demonstrating an established and reasonable biophysical association  
118 with local seasonal temperatures (Wilson et al. 2016). Franke et al. (2020) proposed that the ad-  
119 ditional coverage of the PAGES2k network is preferable to the increased sensitivity of the smaller  
120 NTREND network for global and hemisphere-scale temperature reconstructions but found the  
121 NTREND network provided the best reconstruction in the extratropical Northern Hemisphere. To  
122 produce a maximally skillful reconstruction for this region, we focus on assimilating the NTREND  
123 network but acknowledge that this choice is accompanied by a reduced spatial extent.

124 Before performing an assimilation, we seek to understand the advantages and tradeoffs of offline  
125 EnKF related to both the proxy data and climate model priors. We implement these sensitivity  
126 tests using pseudo-proxy experiments (Mann and Rutherford 2002; Zorita et al. 2003; Smerdon  
127 2012), which allow us to test the DA method’s ability to reconstruct known climate fields within  
128 a controlled setting. Here, we note the importance of model selection in DA pseudo-proxy  
129 experiments and distinguish between “perfect-model” and “biased-model” experimental designs.  
130 In a perfect-model experiment, the same model is used to generate the target field and as the model  
131 prior. Such designs are common in DA analyses (Annan and Hargreaves 2012; Steiger et al. 2014;

132 Okazaki and Yoshimura 2017; Acevedo et al. 2017; Zhu et al. 2020), where they are powerful tools  
133 for testing sensitivity to variables like proxy noise, network distribution, and calibration intervals.  
134 Biased-model paradigms use different climate models to generate target fields and assimilated  
135 model priors and can help examine the effects of biases in a model prior's mean state and spatial  
136 covariance. Dee et al. (2016) found model biases a potentially major source of error in paleo-EnKF  
137 reconstructions, so we employ both perfect and biased-model experiments in our investigations.

138 In this study, we begin by first evaluating the sensitivity of our DA method to proxy noise,  
139 network attrition, and climate model biases in a suite of pseudo-proxy experiments. We also use  
140 the pseudo-proxy framework to compare the skill of our DA method to point-by-point regression  
141 (PPR), the technique used for the original NTREND temperature field reconstruction (Anchukaitis  
142 et al. 2017). We then assimilate the real NTREND tree-ring network to reconstruct mean May  
143 through August (MMJA) temperature anomalies. We produce an ensemble of real reconstructions  
144 by assimilating NTREND with output from multiple climate models in the Coupled Modeling  
145 Intercomparison Project Phase 5 (CMIP5; Taylor et al. 2012) and the Community Earth System  
146 Model (CESM) Last Millennium Ensemble (LME; Otto-Bliesner et al. 2016). We quantify the skill  
147 of the DA reconstructions using spatial temperature anomaly fields, mean Northern Hemisphere  
148 extratropical (30°N–90°N) May through August time series, and withheld proxy data. Finally,  
149 we examine the climate response of the ensemble-mean reconstruction to radiative forcings and  
150 compare these responses against existing temperature field reconstructions.

## 151 **2. Methods**

### 152 *a. Proxy Network*

153 The NTREND network is a curated set of 54 published annual resolution tree-ring based summer-  
154 temperature proxy records selected by dendroclimatologists to maximize sensitivity to boreal  
155 summer temperatures while minimizing the response to other climate variables (Figure 1; Wilson  
156 et al. 2016; Anchukaitis et al. 2017). Although tree growth at the NTREND sites is primarily limited  
157 by summer growing temperatures, the optimal summer season varies between sites. Wilson et al.  
158 (2016) determined the season of highest temperature sensitivity for each site and identified mean  
159 MJJA temperatures anomalies as the optimal reconstruction target for the network as a whole.  
160 The network only includes sites between 40°N and 75°N as lower latitude trees tend to exhibit  
161 sensitivity to multiple climate influences, especially moisture limitations. Each record is derived  
162 from ring-width measurements (TRW), maximum latewood density (MXD; Schweingruber et al.  
163 1978), or a mixture of TRW, MXD, and blue intensity (BI; McCarroll et al. 2002; Björklund et al.  
164 2014; Rydval et al. 2014; Wilson et al. 2019). The network extends from 750 - 2011 CE, with  
165 maximum coverage over the period from 1710-1988 CE. Spatial coverage is greater over Eurasia  
166 (39 sites) than North America (15 sites), with a distinct spatial imbalance prior to 1000 CE (20  
167 vs. 3). We end all reconstructions in 1988 CE as network attrition limits the utility of assimilated  
168 NTREND reconstructions after this point (Anchukaitis et al. 2017).

### 169 *b. Data Assimilation*

170 Our data assimilation method uses an ensemble Kalman filter (EnKF) (Evensen 1994; Steiger  
171 et al. 2014)

$$\mathbf{X}_a = \mathbf{X}_p + \mathbf{K}(\mathbf{Y} - \mathbf{Y}_e) \quad (1)$$

172 to update an initial ensemble of climate states ( $\mathbf{X}_p$ ) given proxy data ( $\mathbf{Y}$ ) and model estimates  
173 of the proxy data ( $\mathbf{Y}_e$ ). These data are combined via the Kalman Gain ( $\mathbf{K}$ ; detailed in Appendix  
174 A1) to produce an updated ensemble ( $\mathbf{X}_a$ ) in each reconstructed annual time step. We use an  
175 EnKF variant known as the ensemble square root Kalman filter (EnSRF; Andrews 1968), with an  
176 “offline” (or “no-cycling”) approach (Oke et al. 2002; Evensen 2003). The complete details of our  
177 approach are given in Appendix A1 and described in Steiger et al. (2014) and Hakim et al. (2016).  
178 The Kalman Filter can be expressed as a recursive Bayesian filter (Chen et al. 2003; Wikle and  
179 Berliner 2007), wherein new information ( $\mathbf{Y}$ ) updates estimates of state parameters ( $\mathbf{X}$ ). Hence, we  
180 will often refer to  $\mathbf{X}_p$  as the model prior, and the updated ensemble  $\mathbf{X}_a$  as the model posterior.

181 We implement a covariance localization scheme, which limits the influence of proxies outside  
182 of a specified radius. Localization was originally developed to limit spurious covariance arising  
183 from sampling noise in small ensembles of  $m \leq 50$  (Houtekamer and Mitchell 2001). Our of-  
184 fline approach enables the use of much larger ensembles ( $m > 1000$ ), but we note that spurious  
185 covariances may still arise from biases in a climate model’s covariance structure. Consequently,  
186 localization may improve the quality of assimilated paleoclimate reconstructions even for large  
187 prior ensembles. The localization radius is an important free parameter in this method and must  
188 be assessed independently for different model priors, reconstruction targets, and proxy networks  
189 (Tables 2, S1). The process used to select localization radii for these experiments is detailed in  
190 Appendix A2.

191 To generate model estimates of the proxy values, we follow the methodology of Tardif et al.  
192 (2019) and use linear univariate forward models trained on the mean temperature of each site’s

193 optimal growing season (Wilson et al. 2016), such that:

$$\mathbf{y}_{e_j} = \alpha_j + \beta_j \mathbf{T}_j. \quad (2)$$

194 Here,  $\mathbf{T}_j$  is a vector of mean growing-season temperature anomalies extracted from the prior. The  
195 coefficients  $\alpha_j$  and  $\beta_j$  are determined by regressing assimilated observations ( $\hat{\mathbf{y}}_j$ ) against mean  
196 growing-season temperature anomalies from the closest grid cell of the target field. We emphasize  
197 that these target fields vary by application. For pseudo-proxy experiments, the target field is a  
198 specific model realization, whereas the real assimilation uses CRU-TS 4.01 (Harris et al. 2014).  
199 Regardless of the target, we perform each regression over the years in which the real NTREND  
200 records overlap data from the closest land grid cell in CRU-TS 4.01; this ensures that both pseudo-  
201 proxy and real reconstructions use regressions with the same temporal span. The variance of  
202 each record’s regression residuals is used as the observation uncertainty ( $R_{jj}$ ) in the Kalman Filter  
203 (Appendix A1). This uncertainty ranges from 0.23 to 1.34 proxy units over the network.

204 We construct prior ensembles using output from the past1000 and historical experiments of the  
205 Coupled Modeling Intercomparison Project Phase 5 (CMIP5; Taylor et al. 2012) as well as the Last  
206 Millennium Ensemble (LME; Otto-Bliesner et al. 2016). For a given assimilation, we use values  
207 from a single climate model and designate each year of available output as a unique ensemble  
208 member. We use static model priors, whereby the same prior is used for each reconstructed time  
209 step. This scheme is justified by the limited forecast skill of climate models beyond the annual  
210 reconstruction timescale (Bhend et al. 2012) and is common in paleo-DA applications (e.g. Steiger  
211 et al. 2014; Dee et al. 2016; Tardif et al. 2019). A summary of the model ensembles is given in Table  
212 1. The past1000 CMIP5 data for each model are from the ensemble member designated *r1i1p1*, and  
213 LME output was selected from full-forcing run 2. We assimilate temperature anomalies relative to  
214 the 1951-1980 CE mean; this helps avoid the effects of climate model mean state biases, but we

215 note that model covariance biases are unaffected. In all reconstructions, we update the mean May  
 216 through August (MJA) temperature anomaly field, rather than individual months. We assess the  
 217 skill of each assimilation by comparing the Pearson’s correlation coefficients, root mean square  
 218 errors (RMSEs), mean biases, and standard deviation ratios.

219 *c. Pseudo-proxy Reconstructions*

220 Before assimilating the real NTREND network, we first examine the skill of our DA method in a  
 221 pseudo-proxy framework (Smerdon 2012). This approach allows us to test the method’s ability to  
 222 reconstruct known climate field targets within a controlled setting. Here, we specify the target fields  
 223 as surface temperatures from the years 850-2005 CE from either the Last Millennium Ensemble  
 224 full-forcing run 2 (CESM; Otto-Bliesner et al. 2016), or from the combined last millennium  
 225 and historical runs of the Max Planck Institute for Meteorology Earth System Model (MPI;  
 226 Marsland et al. 2003; Stevens et al. 2013). While this experimental design is intentionally tractable,  
 227 we caution that the observed spatial patterns of skill will depend on the specific models used  
 228 (Smerdon et al. 2011). Here, we are interested in examining the sensitivity of EnSRF to the proxy  
 229 network and climate model prior, so we systematically explore the effects of noisy proxy records,  
 230 network attrition, and biased climate models on DA performance. To examine the effects of model  
 231 covariance biases, we test each combination of target field and model prior for LME and MPI,  
 232 which allows us to alternate between perfect-model and biased-model experimental designs.

233 After selecting a target field, we generate pseudo-proxies using:

$$\hat{\mathbf{y}}_j = a_j + b_j \mathbf{T}_j^{\text{target}} + \epsilon_j \quad (3)$$

234 where  $\hat{\mathbf{y}}_j$  is the  $j^{\text{th}}$  pseudo-proxy record and  $\mathbf{T}_j^{\text{target}}$  is the vector of mean growing season temperature  
 235 anomalies from the grid cell closest to the proxy site in the target climate field. The coefficients  $a_j$

236 and  $b_j$  are the intercept and slope obtained by regressing the real NTREND network against mean  
 237 growing-season temperature anomalies from the nearest land cells in CRU-TS 4.01; in this way,  
 238 the pseudo-proxies mimic the temperature response of the real NTREND network for at least the  
 239 instrumental period.

240 We examine the effects of proxy noise by selectively neglecting or adding Gaussian white noise  
 241 to the pseudo-proxies, such that:

$$\epsilon_j \sim \begin{cases} 0, & \text{Perfect} \\ \mathcal{N}(0, R_{jj}), & \text{Noisy} \end{cases} \quad (4)$$

242 Here,  $R_{jj}$  is the proxy-uncertainty weight for the  $j^{\text{th}}$  NTREND record and is the variance of the  
 243 NTREND-CRU regression residuals. When testing noisy proxies, we perform 101 assimilations  
 244 using different noise matrices and report the median skill metrics. Here, we use white noise because  
 245 it allows us to directly tune the  $R_{jj}$  weight in the Kalman Filter. The median signal-to-noise ratio  
 246 is 0.80 for the CESM pseudo-proxies and 0.85 for the MPI pseudo-proxies, which is consistent  
 247 with values found in other pseudo-proxy experiments (Smerdon 2012). In each test, we examine  
 248 the effects of network attrition by first assimilating the full set of pseudo-proxies over the entire  
 249 period and then comparing this to an assimilation where the pseudo-proxies are subjected to the  
 250 same temporal attrition as the real NTREND network.

251 After generating pseudo-proxies for a given experiment, we generate pseudo-proxy estimates  
 252 by applying equation 2 to the prior ensemble. The coefficients  $\alpha_j$  and  $\beta_j$  are determined by  
 253 regressing the pseudo-proxies against the target field. Note that pseudo-proxy noise and sampling  
 254 errors will affect the statistics obtained from these regressions, so  $\alpha_j$  and  $\beta_j$  are estimates of the  
 255 coefficients  $a_j$  and  $b_j$  used to generate the pseudo-proxies. This mimics how noise and sampling  
 256 errors can introduce errors into forward models calibrated on real NTREND data. Once we obtain

257 pseudo-proxy estimates, we then determine an optimal localization radius (Appendix A2, Table  
258 S1).

259 A key feature of pseudo-proxy experiments is that the target reconstruction is known. Conse-  
260 quently, we can assess skill directly against the correct answer. Here, we examine pseudo-proxy  
261 reconstruction skill using mean Northern Hemisphere extratropical (30°N–90°N) MJJA tempera-  
262 ture time series, and spatial grid point time series over the full reconstruction period (850 CE to  
263 1988 CE).

264 We compare the most realistic (biased-model, noisy-proxy, temporal-attrition) pseudo-proxy DA  
265 reconstructions to analogous reconstructions generated using point-by-point regression (PPR). PPR  
266 is a “region of interest” CFR technique that iteratively calculates a nested multivariate principal  
267 components regression model between predictor network and each point in the target field (Cook  
268 et al. 1999). The method was motivated by the premise that proxies near a reconstructed grid  
269 point are more likely to reflect climate at that site. Consequently, PPR uses a strict search radius  
270 to select proxy predictor series for each grid point reconstruction. The method was first used for  
271 drought reconstructions (Cook et al. 1999, 2010a,b) and later adapted for continental temperature  
272 anomalies (Cook et al. 2013). Anchukaitis et al. (2017) used the method to reconstruct hemispheric  
273 temperature anomalies, and we follow their implementation in this study.

274 In brief, given a target of gridded climate observation, the method first identifies proxy sites  
275 within 1000 km of each grid point centroid. If no proxy records are found within 1000 km, the  
276 search radius is expanded in 500 km increments to a maximum of 2000 km until proxy sites are  
277 found within the radius. All proxy sites found within the search radius are then used as predictor  
278 sites for that grid point. If no predictors are found within 2000 km, then no reconstruction is  
279 performed for the grid. These radii are based on decorrelation decay lengths in the observational  
280 temperature field from Cowtan and Way (2014). A multivariate regression model is then calibrated

281 against the MJJA temperature values of the target field (Cowtan and Way 2014) for each grid point  
282 over the period 1945 to 1988 CE, and the reconstructions are validated using withheld temperature  
283 data for the period 1901 to 1944 CE. As the number of records declines back through time, the  
284 regression model is recalibrated and validated for each change in network size and scaled to match  
285 the mean and variance of the predictand during their overlapping time period (Meko 1997; Cook  
286 et al. 1999). For a given grid point, temperature anomalies are obtained for all years in which at  
287 least one predictor record remains within the initial search radius. Following Anchukaitis et al.  
288 (2017), we then screen the final reconstructed field in each time step to only include grid cells  
289 where the reduction of error (RE; Cook et al. (1994)) statistic is greater than zero. We use this  
290 screened field here as the final PPR MJJA temperature reconstruction.

#### 291 *d. Real NTREND Reconstruction*

292 We next assimilate the real NTREND network. To examine the effects of prior selection, we  
293 produce 10 real DA reconstructions each using a different climate model to generate the prior (Table  
294 1). Since each prior is itself an ensemble, these 10 reconstructions effectively create an ensemble  
295 of ensembles. To minimize ambiguity, we will henceforth refer to the set of 10 reconstructions  
296 as the “multi-model ensemble”, and the DA ensemble for each individual reconstruction as a  
297 “prior/posterior ensemble”.

298 Forward model estimates of the NTREND records in each reconstruction are determined by  
299 applying equation 2 to CRU-TS 4.01. We assess the skill of each reconstruction using time-series  
300 of mean Northern Hemisphere extratropical (30°N–90°N) MJJA temperature, instrumental spatial  
301 field grid points, and independent proxy records. The skill of the extratropical time series is  
302 determined using a Monte Carlo calibration-validation procedure (Appendix A2). Spatial skill is  
303 computed against the Berkeley Earth surface temperature field (BEST; Rohde et al. 2013) over

304 the period 1901 - 1988 CE. The BEST instrumental record is not used in the forward model and  
 305 localization calibrations, which instead leverage the CRU product. However, we caution that BEST  
 306 is not a truly independent dataset, as both BEST and CRU are partly based on the same instrumental  
 307 climate data. As an additional validation we assess the ability of DA to reconstruct withheld proxy  
 308 time series. We perform a series of leave-one-out assimilations for each model by iteratively  
 309 removing a single proxy time-series from the NTREND network and assimilating the remaining  
 310 53 records. In these experiments, we construct the prior from the average temperatures over the  
 311 removed site's optimal growing season at the grid point closest to the removed site. This allows us  
 312 to apply Equation 2 to the posterior to estimate the removed record from the reconstruction. We  
 313 then compare this estimate to the real withheld NTREND record.

314 We next calculate a mean reconstruction for the multi-model ensemble. To do so, we first  
 315 calculate ensemble-mean values from the posterior of each of the reconstructions. The mean of  
 316 the multi-model ensemble is then calculated as the mean of these 10 posterior ensemble means.  
 317 We quantify uncertainty of the multi-model mean using first the mean of the 10 posterior ensemble  
 318 widths:

$$\sigma_{\text{multi-model mean}}^2 = \frac{1}{10} \sum_{i=1}^{10} \sigma_{\text{posterior ensemble } i}^2 \quad (5)$$

319 and then the  $2\sigma$  width of the multi-model ensemble for the series. We first determine the multi-  
 320 model ensemble-mean for the extratropical MJJA time series. We next compute a mean spatial  
 321 reconstruction for the multi-model ensemble by linearly interpolating each reconstruction to the  
 322 lowest model resolution and averaging at each grid point.

323 We compare the multi-model mean spatial product to several recent temperature CFRs sum-  
 324 marized in Table 3. In brief, Guillet et al. (2017) focused on reconstructing high-frequency  
 325 temperature anomalies associated with known volcanic eruptions using a network of a similar size  
 326 and composition to the NTREND network in a linear regression framework and their work provides

327 a comparison point with Anchukaitis et al. (2017). The LMR 2.1 reconstruction applied an offline  
328 EnSRF DA to the PAGES2k network and allows us to compare DA reconstructions using different  
329 proxy networks (Tardif et al. 2019). From Zhu et al. (2020), we examine the reconstruction of  
330 mean June through August (JJA) temperatures using PAGES2k trees. The Neukom et al. (2019)  
331 DA offers another comparison point, using a proxy network of intermediate size derived from a  
332 screened version of PAGES2k. Neukom et al. (2019) performed an ensemble of reconstructions  
333 using different methods and recommend using the ensemble mean reconstruction for climate anal-  
334 ysis; however, we only focus on the DA product to emphasize the differences in reconstructions  
335 that arise when using similar methodologies.

336 We examine the temperature response to external forcing for both the reconstruction ensemble and  
337 temperature CFRs. We compare temperature anomalies between the Medieval Climate Anomaly  
338 (MCA; 950 - 1250 CE) and the Little Ice Age (LIA; 1450 - 1850 CE) (Masson-Delmotte et al. 2013;  
339 Anchukaitis et al. 2017), and separately use superposed epoch analysis (Haurwitz and Brier 1981) to  
340 determine composite mean responses to major tropical volcanic eruptions. For the volcanic events,  
341 we follow Sigl et al. (2015) and identify years containing a global eruption forcing magnitude equal  
342 to or larger than the 1884 Krakatoa eruption ( $n = 20$ ), which yields the following event years: 916,  
343 1108, 1171, 1191, 1230, 1258, 1276, 1286, 1345, 1453, 1458, 1595, 1601, 1641, 1695, 1809, 1815,  
344 1832, 1836, and 1884 CE (Sigl et al. 2015; Anchukaitis et al. 2017). We calculate temperature  
345 anomalies relative to the mean of the five years preceding each of these event years.

### 3. Results

#### *a. Pseudo-proxy experiments*

The pseudo-proxy reconstructions are most skillful in the extratropical Northern Hemisphere (Figure 2). In this region, ocean basin correlations are lower relative to land with notable exceptions over the eastern and north-western edges of the Pacific. Correlations generally decline with increasing distance from the extratropical Northern Hemisphere and the tree-ring network, although significant spatial heterogeneity exists throughout the tropics. The climate model covariance biases cause the largest reductions in correlation coefficients and sharply reduce skill outside of the extratropical Northern Hemisphere. Network attrition and proxy noise have comparatively minor effects over the full period. Results for other skill metrics show similar behavior (Figures S1, S2, and S3).

We next compare the most realistic (biased-model, noisy-proxy, temporal-attrition) DA experiments to PPR reconstructions. Given the strict reconstruction radius in PPR, and the spatial pattern of DA skill, we consider only the extratropical Northern Hemisphere in our discussion. The skill metrics for the mean extratropical time series are similar for the two methods (Table S2; Figures S4, S5). The regional spatial correlations of the DA and PPR reconstructions for the CESM and MPI targets (Figures 3 and S6, respectively) are also comparable: each exhibits correlations with the target field greater than 0.7 in Scandinavia, western Siberia, and western Canada, and these regions correspond to the best coverage by the proxy network. Similarly, both methods exhibit low correlations in southeastern Canada, eastern Siberia, and in the region of the Black and Caspian Seas. The DA does however exhibit a broader spatial region of high correlation than PPR, and DA correlations are higher than PPR values at nearly all grid points. Similarly, DA reconstructions exhibit lower RMSE values at most grid points. Standard deviation ratios indicate that the DA

369 reconstructions underestimate temporal temperature variability, but this effect is less severe near  
370 the proxy sites. In contrast with DA, PPR time series  $\sigma$  ratios neither strictly overestimate nor  
371 strictly underestimate temporal variability, instead demonstrating a mixed response over the hemi-  
372 sphere. In general, our DA reconstructions underestimate variability more strongly than the PPR  
373 analogues. Mean biases are comparable, with both methods exhibiting similar spatial patterns and  
374 bias magnitudes, although it is interesting to note that the spatial patterns of bias change markedly  
375 depending on the target field.

### 376 *b. Real NTREND Reconstruction*

377 For the real NTREND data assimilation, validation statistics for the mean extratropical MJJA  
378 time series are similar across all priors (Table 2) with mean correlations of 0.70, RMSE of 0.19 °C,  
379 and absolute mean bias of 0.06 °C. Temporal variability is close to the target with mean standard  
380 deviation ratios of 1.11. Time series obtained using different model priors (Figure S7) have a  
381 mean range of 0.22 °C over the period of full coverage (1750-2988 CE;  $n = 54$ ). However, the  
382 reconstructed time series diverge as the network becomes sparse, with a range of 0.76 °C by the  
383 first year of the reconstruction (750 CE;  $n = 4$ ). The model ensemble-mean time series exhibits  
384 similar skill values as the reconstructions for the individual models (Table 2) with a correlation of  
385 0.72, RMSE of 0.18 °C, temporal  $\sigma$  ratio of 1.06, and a mean bias of 0.05 °C.

386 We compare the extratropical MJJA time series for the multi-model mean to analogous time  
387 series extracted from the Berkeley Earth (BEST) instrumental record and the Anchukaitis et al.  
388 (2017) NTREND PPR reconstruction (Figure 4). The DA series shows similar behavior to BEST  
389 from 1880-1988 CE, although both the DA and PPR reconstructions of Anchukaitis et al. (2017)  
390 diverge from this dataset over the earliest period from 1850-1879 CE. This may reflect a warm  
391 bias (Parker 1994; Frank et al. 2007; Böhm et al. 2010) and limited spatial coverage (Rohde et al.

392 2013; Anchukaitis et al. 2017) in the early instrumental temperature record. The DA and PPR  
393 time series show similar behavior over most of the record, with a correlation coefficient of 0.88.  
394 Temporal variability is generally higher in the PPR series than in the DA. Prior to about 1100 CE,  
395 the series' running standard deviations show larger differences, which is caused by the decrease in  
396 DA reconstructed variability.

397 Most spatial validation statistics show similar patterns to those observed in the pseudo-proxy  
398 experiments (Figure 5). Correlation coefficients and standard deviation ratios indicate the highest  
399 skill over Scandinavia, central and northern Asia, and northwestern North America, the regions  
400 of densest network coverage. Correlation coefficients approach 0.8 and standard deviation ratios  
401 approach 1 near the proxy sites themselves. Over land, mean biases are typically below 0.5  
402 °C, with the largest largest over central Canada and eastern Siberia and smallest over the Arctic  
403 Archipelago, Alaska, and west-central Asia. Away from the proxy sites, temporal variability is  
404 underestimated, particularly over the oceans. However, most land grid points exhibit  $\sigma$  ratios near  
405 1 with a slight overestimate in central Asia and northern Japan. Much of the temporal variability in  
406 the extratropical mean time series is driven by land grid points, and this tendency helps reconcile  
407 Figure 5 with extratropical mean time series  $\sigma$  ratios near 1. RMSE values are typically less than  
408 0.6 °C, but rise to values near 1 °C over the North Pacific, central Canada, and north of the Caspian  
409 Sea.

410 Independent proxy validation statistics (Table 4) show median correlation coefficients near 0.5,  
411 and RMSE values near 1°C. Temporal variability is underestimated relative to the target series  
412 with  $\sigma$  ratios typically between 0.3 and 0.4. Mean biases are variable and depend on the prior  
413 model used. Not surprisingly given the sparsity of the NTREND network, removing even a single  
414 proxy record from the assimilation can substantially reduce the ability to reconstruct temperature  
415 anomalies at nearby grid cells. Consequently, the leave-one-out assimilation process we use

416 to assess independent proxy skill almost certainly underestimates overall field validation skill.  
417 Nevertheless, these values are comparable to previous efforts with median correlation coefficients  
418 somewhat higher than those in Hakim et al. (2016) and Tardif et al. (2019).

### 419 *c. Epochal Temperature Changes*

420 We next examine the temperature change between the Medieval Climate Anomaly (MCA; 950  
421 - 1250 CE) and the Little Ice Age (LIA; 1450 - 1850 CE) (Masson-Delmotte et al. 2013; An-  
422 chukaitis et al. 2017). The reconstructions nearly all indicate warmer temperatures during the  
423 MCA throughout the high latitudes with maximum anomalies typically over northeastern Canada  
424 (Figure 6). However, anomaly magnitudes vary across reconstructions with values ranging from  
425 over 1.6 °C (for CCSM4, MIROC, MPI priors) to less than 0.8 °C (IPSL and FGOALS priors).  
426 The spatial pattern also varies by model prior. Many reconstructions show stronger anomalies in  
427 Fennoscandia, northeastern Asia, and northwestern North America, but these patterns do not occur  
428 in all models.

429 Comparing the MCA-LIA difference for our multi-model mean reconstruction with other CFRs  
430 (Figure 7), we find our spatial anomaly patterns most similar to Anchukaitis et al. (2017). Anomaly  
431 magnitudes are also comparable, except over northeastern Canada. In the Anchukaitis et al. (2017)  
432 reconstruction, this region exhibits anomalously high medieval temperatures ( $> 3$  °C), which  
433 they attribute to a detrending artifact in a tree-ring record from Quebec. By contrast, our DA  
434 reconstruction produces a maximum medieval anomaly of 1 °C for this region, in better agreement  
435 with other proxy reconstructions (e.g. 0-1.5°C; Sundqvist et al. 2014). Comparing the results  
436 of this study to Neukom et al. (2019), we observe that both NTREND DA and Neukom et al.  
437 (2019) exhibit a positive anomaly over most of the high-latitude Northern Hemisphere; however,  
438 the anomalies in the Neukom et al. (2019) product have much larger magnitudes and the maxima

439 of the North America features occur in different locations. Zhu et al. (2020) also indicate positive  
440 anomalies in the Northern Hemisphere, but these are lower magnitude than the other products  
441 and more spatially localized. By contrast, the LMR2.1 product (Tardif et al. 2019) exhibits an  
442 anomaly pattern notably different from the other reconstructions, with a strong positive anomaly in  
443 the Arctic Ocean north of Siberia. Since the Guillet et al. (2017) reconstruction reflects high-pass  
444 filtered reconstructed temperatures, we do not consider it in this comparison.

#### 445 *d. Volcanic Response*

446 We next examine the composite mean response to major tropical volcanic eruptions. Our 10  
447 reconstructions show broadly similar responses to large tropical volcanic eruptions (Figure 8), with  
448 the spatial pattern characterized by a strong cold anomaly in northern Canada and a second region  
449 of cooling extending from Fennoscandia east of the Caspian Sea toward central Asia. However,  
450 the extent and magnitude of these vary between the different reconstructions. Several regions also  
451 exhibit markedly different spatial patterns across the 10 reconstructions. In particular, the response  
452 in central North America and eastern Asia appears highly sensitive to the choice of model prior.

453 Comparing the volcanic pattern for our multi-model mean reconstruction with the other existing  
454 CFRs (Figure 9) shows large differences in spatial patterns, magnitudes, and even sign of the  
455 anomalies. In general, most CFRs show some combination of cooling anomalies in northern  
456 North America and northern Asia, with a slight neutral or warming anomaly in the North Pacific.  
457 However, these features are not present in all the CFRs and vary in maximum magnitude. The mean  
458 of our model ensemble, Anchukaitis et al. (2017), and Guillet et al. (2017) products all exhibit  
459 the northern Canada and western Asia cooling features and the spatial extent is similar for the two  
460 NTREND products. In contrast, the Guillet et al. (2017) Canadian feature is centered farther east,  
461 and its northern Asian feature is stronger (near 1.5 °C) with a maximum more strongly localized to

462 northern Siberia. These two features are also present in Zhu et al. (2020), but maximum cooling is  
463 smaller in magnitude. The LMR2.1 does not show distinct north Asian terrestrial cooling, although  
464 an anomaly of 0.6 C is reconstructed in the Arctic Ocean north of Siberia. This reconstruction  
465 also demonstrates a North American response pattern similar to Zhu et al. (2020) with a reduced  
466 magnitude of cooling in northern Canada. The Neukom et al. (2019) product again shows the largest  
467 anomalies, with values greater than 1.5 °C over much of northern Siberia and Fennoscandia. This  
468 feature does not extend as far south as in the NTREND DA ensemble-mean but is zonally wider.  
469 Neukom et al. (2019) also show a single strong North American feature with cooling magnitudes  
470 near 1.2 °C. Interestingly, Neukom et al. (2019) exhibits a North Pacific warming response that  
471 strengthens one year after the volcanic event, a feature also evident in the Anchukaitis et al. (2017)  
472 reconstruction that may reflect changes in atmospheric circulation following an eruption (e.g.  
473 Robock 2000; Stenchikov et al. 2006; Christiansen 2008; Schneider et al. 2009)

#### 474 **4. Discussion**

475 The pseudo-proxy experiments indicate that regions of high reconstruction skill for the assim-  
476 ilated NTREND network is limited to the extratropical Northern Hemisphere when using biased  
477 climate model priors. This finding supports work by Franke et al. (2020) and suggests that analyses  
478 of temperatures using the NTREND network should be limited to this region, consistent with  
479 Wilson et al. (2016) and Anchukaitis et al. (2017). In comparison with Anchukaitis et al. (2017)  
480 (NTREND PPR), our DA method exhibits similar skill at reconstructing mean Northern Hemi-  
481 sphere extratropical MJJA time series using the NTREND network, but also provides continuous  
482 field estimates of past temperature and improves the spatial correlation and RMSE. We suggest this  
483 improvement arises at least in part from the contrast between PPR's strict-limited search radius and  
484 the DA's longer localization radii. Many NTREND sites exhibit statistically significant covariance

485 with the MJJA temperature field outside of PPR's 2000 km maximum search radius (see Figure  
486 5 of Anchukaitis et al. (2017)), and these distal covariances are not used to improve the PPR  
487 reconstruction. By contrast, the DA uses no localization in these pseudo-proxy experiments (Table  
488 S1) and if the model prior provides a good estimate of a proxy site's field covariance, the proxy  
489 record can inform the reconstruction of distal grid points. Ultimately, these results suggest that  
490 our DA method improves on the spatial component of Anchukaitis et al. (2017) for reconstructing  
491 a Northern Hemisphere temperature history of the Common Era from the NTREND network. We  
492 note that, as is the case for most field reconstruction methods (Ammann and Wahl 2007; Tingley  
493 et al. 2012), our offline DA method implicitly assumes the broad-scale covariance patterns can be  
494 considered stationary through time. Transient offline (e.g. Bhend et al. 2012; Valler et al. 2019;  
495 Franke et al. 2020) or online assimilation techniques (e.g. Perkins and Hakim 2017) may offer  
496 additional improvements.

497 Our results also highlight the sensitivity of the DA reconstructions to the model prior. In the  
498 pseudo-proxy experiments, the introduction of model covariance bias reduces widespread global  
499 skill to the high latitude Northern Hemisphere and the regions nearest the proxy sites. Network  
500 attrition and proxy noise cause comparatively small effects over the full period, a finding in  
501 agreement with Dee et al. (2016). Given this potential for perfect-model experiments to exaggerate  
502 the magnitude and spatial extent of DA skill, we encourage future DA proof-of-concept and  
503 sensitivity studies to consider perfect-model experiments in conjunction with biased-model cases.  
504 In contrast with these results, previous assimilation efforts have found little sensitivity to the  
505 choice of prior (Hakim et al. 2016). The small size of the NTREND network may exacerbate this  
506 sensitivity, but even assimilations using larger networks may be sensitive to the choice of priors in  
507 those periods with reduced proxy coverage.

508 Reconstructions are most sensitive to the prior when the proxy network becomes small. For  
509 example, despite using the same proxy network and reconstruction technique, mean extratropical  
510 MJJA temperature time series diverge by more than 0.5 °C in the earliest parts of the reconstruction  
511 when the number of sites in our network is limited (Figure S7). The use of different priors also  
512 produces noticeable differences in spatial MCA-LIA temperature anomaly patterns (Figure 6),  
513 which we interpret as arising from the reduced size of the proxy network during the MCA. In  
514 contrast, the volcanic response maps present a more consistent spatial pattern (Figure 8), which we  
515 attribute to the larger size of the proxy network during most of the volcanic events. The magnitude  
516 of the forced response may also contribute to similarity across the priors; however, the volcanic  
517 response maps still exhibit different spatial patterns in regions like east Asia where the proxy  
518 network is sparse.

519 The consistency with which the DA underestimates the temporal variability of the target field,  
520 particularly over the oceans and far from the proxy sites, requires consideration. In this study,  
521 we focus on time series derived from the posterior ensemble-mean at each time step. However,  
522 this focus on the ensemble-mean neglects the width of the full posterior ensemble. Like many  
523 offline EnSRF studies (e.g. Hakim et al. 2016; Dee et al. 2016; Steiger et al. 2018), our method  
524 uses a stationary prior in each time step; thus, the prior ensemble-mean is constant through time.  
525 As the proxy network becomes sparse, update magnitudes decrease, and the posterior ensemble  
526 more closely resembles the prior. When this occurs, the reconstructed ensemble-mean time series  
527 will closely resemble the mean of the prior ensemble, and the time series' temporal variability  
528 will approach zero. Similarly, regions far from the proxy network will exhibit smaller update  
529 magnitudes, so grid point time series far from the proxy sites have lower  $\sigma$  ratios. However,  
530 this reduction in temporal variability is balanced by increased posterior ensemble width, which  
531 will remain near the spread of the prior ensemble. Incorporating the width of the posterior with

532 ensemble-mean time series can produce a range that encompasses target time-series variability,  
533 but it is not always clear how to use these ranges in spatiotemporal analyses. Hence, we emphasize  
534 that users of DA products with constant priors should carefully consider how changes in the proxy  
535 network affect the temporal variability of posterior ensemble-mean time series and make use of  
536 the posterior range when possible. We also note that allowing the model prior to vary in each time  
537 step may help mitigate these effects, which again may argue for expanded future use of transient  
538 offline priors (e.g. Bhend et al. 2012; Valler et al. 2019; Franke et al. 2020) or online assimilation  
539 techniques (e.g. Perkins and Hakim 2017) where possible.

540 The prior sensitivity and temporal variability effects underscore the importance of understanding  
541 how the proxy network affects the quality of the reconstruction (Esper et al. 2005; Wang et al.  
542 2014). A key feature of DA techniques is the ability to estimate reconstruction uncertainty in each  
543 time step from the width of the posterior ensemble. Figure 10 provides an example of such an  
544 analysis for the multi-model mean by examining the temperature response following the 1257 CE  
545 (Lavigne et al. 2013) and 1600 CE (De Silva and Zielinski 1998) volcanic eruptions in conjunction  
546 with the full posterior width. The uncertainty maps for both events show maxima in central North  
547 American and northeastern Asia and suggest that associated temperature anomalies should be  
548 interpreted more cautiously. Notably, these regions correspond to areas that are also sensitive to  
549 the prior in Figure 8. By contrast, central and east-central Asia, Fennoscandia, central Europe, and  
550 southwestern Canada exhibit a narrow posterior for both events, so volcanic anomalies in these  
551 regions are better constrained. Interestingly, the temperature response in 1601 CE is relatively  
552 small over much of central Europe and reconstruction uncertainty is relatively low, which suggests  
553 this feature may be a robust feature of the post-eruption climate anomaly. In addition to supporting  
554 analysis of reconstructed climate features, these uncertainty estimates can help identify regions  
555 that would benefit from increased network density (Comboul et al. 2015). In particular, we observe

556 that northern North America and eastern Siberia would benefit from the development of new  
557 millennial-length temperature-sensitive tree-ring records.

558 The CFR comparison reveals the highly variable nature of spatial patterns and magnitudes of  
559 reconstructed temperature anomalies that result from different selections of proxy networks, target  
560 fields, and reconstruction methodologies. For example, despite using the same proxy network  
561 and target field, the DA multi-model mean and PPR result from Anchukaitis et al. (2017) have  
562 MCA-LIA anomalies that differ by over 2 °C in northeastern Canada (Figure 7), which relates to the  
563 outsized effect of the Quebec tree-ring width record (Gennaretti et al. 2014) on the Anchukaitis et al.  
564 (2017) reconstruction. We note that the localization radii used in our reconstructions ( $\geq 9500$  km)  
565 allow proxies to influence grid cells farther away than the maximum 2000 km search radius used by  
566 Anchukaitis et al. (2017), so distant proxies are able to counter the effects of the Quebec record in  
567 the DA. Even within the same DA framework, our results indicate that reconstructed temperature  
568 responses are highly variable, particularly for MCA-LIA anomalies. These differences result from  
569 targeting different fields and leveraging different proxy networks. Aside from spatial and temporal  
570 coverage, we note that using proxy records that are not strictly temperature sensitive can introduce  
571 structural biases relative to other temperature CFRs. For example, the LMR2.1 reconstruction  
572 includes proxies that are sensitive to more than just temperature, which could possibly reduce  
573 update magnitudes and help explain the smaller magnitudes of the volcanic responses. Similarly, the  
574 Neukom et al. (2019) DA product and LMR2.1 incorporate proxies like corals and lake-sediments  
575 that are not present in the tree-ring based CFRs, and it is possible that these records influence  
576 the large magnitudes of the Neukom et al. (2019) DA climate responses or the atypical LMR2.1  
577 MCA-LIA spatial pattern. However, we emphasize that these hypotheses are strictly speculative  
578 at this moment and that the differences in reconstructed climate response by themselves do not  
579 indicate whether one proxy network or reconstruction is superior to another in representing past

580 climate variability. Instead, our CFR comparison highlights that, despite the recent decades of  
581 progress in understanding both methods and paleoclimate data (Hughes and Ammann 2009; Frank  
582 et al. 2010; Smerdon et al. 2011; Tingley et al. 2012; Wang et al. 2014; Smerdon and Pollack  
583 2016; Christiansen and Ljungqvist 2017; Esper et al. 2018), differences in reconstructions of past  
584 temperature still arise when using different proxy networks, different target seasons, and making  
585 different reconstruction choices, and these differences fundamentally influence our interpretation  
586 of the temperature response to radiative forcing (c.f. Wang et al. 2015). This observation calls for  
587 a revival of paleo-reconstruction intercomparison projects (e.g. Ammann 2008; Graham and Wahl  
588 2011; Anchukaitis and McKay 2015) in order to examine the behavior, strengths, and weaknesses of  
589 different proxy networks and reconstruction choices in a systematic and community-driven manner.  
590 Furthermore, such an effort would help identify regions with consistently large reconstruction  
591 uncertainties and indicate where to prioritize the development of new or the extension of existing  
592 tree-ring records.

## 593 **5. Conclusions**

594 In this study, we assimilate a small but highly temperature-sensitive tree-ring network based on  
595 expert assessment to reconstruct summer (MJJA) temperature anomalies from 750-1988 CE. Our  
596 method is skillful in the extratropical Northern Hemisphere and improves on a previous spatial  
597 reconstruction using the same network, thereby providing a new dataset with which to examine  
598 temperature dynamics and climate response to radiative forcing over the last millennium. In a set  
599 of pseudo-proxy experiments, we find that our method is sensitive to climate model biases, so we  
600 perform an ensemble of reconstructions using 10 different climate model priors. Reconstructed  
601 temperature anomalies are sensitive to the selection of the model prior when the proxy network  
602 becomes sparse, but the reconstructed spatial patterns and time series converge to consistent values

603 as the number of sites in the NTREND proxy network increases. As one consequence of using static  
604 offline priors, our method underestimates temporal variability particularly when the proxy network  
605 becomes small, which argues for the future use of transient offline priors, online assimilation  
606 techniques in DA paleoclimate reconstructions, and expanded proxy development. There is also  
607 a need for continued development of proxy system forward models, particularly for the important  
608 MXD metric. The influence of the proxy network coverage on the reconstructions emphasizes the  
609 importance of analyzing reconstructed temperature anomalies in conjunction with estimates of their  
610 uncertainty. These uncertainty estimates emerge naturally for both spatial fields and time series  
611 from the DA posterior ensembles and are an enhancement over previous reconstructions using the  
612 NTREND dataset. In addition to gauging reconstruction validity, the uncertainty estimates identify  
613 regions that would benefit from additional proxy records and support the development of more  
614 millennial-length temperature-sensitive tree-ring records in treeline North America and eastern  
615 Siberia especially. Comparison of our reconstruction with other temperature CFRs indicates that  
616 reconstructed temperature anomalies have highly variable spatial patterns and magnitudes, even  
617 within similar reconstruction frameworks and proxy network. These different climate responses  
618 call for a renewed paleo-reconstruction intercomparison framework in which to systematically  
619 examine the effects of network selection across reconstruction techniques and prioritize regions  
620 for future record development.

621 *Data availability statement.* The NTREND proxy data and the earlier reconstructions are avail-  
622 able from the NOAA NCEI World Data Service for Paleoclimatology ([https://www.ncdc.  
623 noaa.gov/paleo-search/study/19743](https://www.ncdc.noaa.gov/paleo-search/study/19743)). The NTREND-DA ensemble reconstructions will  
624 be available from NOAA NCEI World Data Service for Paleoclimatology ([insert url here once  
625 accepted]). Model priors from the CMIP5 and CESM LME are available on the Earth System

626 Grid (<https://esgf-node.llnl.gov/projects/esgf-llnl/>) and the NCAR Climate Data  
627 Gateway (<https://www.earthsystemgrid.org/>), respectively. The data and code used to run  
628 these analyses and a function reproducing the results and figures from this paper are available at  
629 <https://doi.org/10.5281/zenodo.3989941>.

630 *Acknowledgments.* The authors acknowledge support from the Climate Program Office of the  
631 National Oceanographic and Atmospheric Administration (NOAA grants NA18OAR4310420 to  
632 KJA, NA18OAR4310426 to JEG and FZ, and NA18OAR4310422 to GJH). GJH also acknowledges  
633 support from the NSF through grant AGS-1702423. JMK and KJA were supported by NSF grant  
634 AGS-1803946. JET and JMK acknowledge support from NSF grant #AGS-1602301 and Heising-  
635 Simons Foundation grant #2016-05. We acknowledge the World Climate Research Programme's  
636 Working Group on Coupled Modelling, which is responsible for CMIP, and we thank the climate  
637 modeling groups (listed in Table 1 of this paper) for producing and making available their model  
638 output.

## Data Assimilation Methods

### A1. The Ensemble Kalman Filter

Our data assimilation method uses an ensemble Kalman filter approach (Evensen 1994; Steiger et al. 2014; Hakim et al. 2016) to solve the update equation:

$$\mathbf{X}_a = \mathbf{X}_p + \mathbf{K}(\mathbf{Y} - \mathbf{Y}_e) \quad (\text{A1})$$

in each reconstructed annual time step. Here  $\mathbf{X}_p$  is an initial ensemble of plausible climate states, an  $n \times m$  matrix where  $n$  is the number of state variables and  $m$  is the number of ensemble members.  $\mathbf{X}_a$  is the updated ensemble (the analysis), also an  $n \times m$  matrix.  $\mathbf{Y}$  is a  $d \times m$  matrix of observed proxy values, where  $d$  is the number of available proxy records in a given time step.  $\mathbf{Y}_e$  is a  $d \times m$  matrix consisting of model estimates of the proxy values. Each row  $y_{e_j}$  is determined by applying the forward model for the  $j^{\text{th}}$  proxy site to the ensemble via Equation 2.  $\mathbf{K}$  is the Kalman Gain, an  $n$  by  $d$  matrix that weights the covariance of proxy sites with the target field by the uncertainties in the proxy observations and estimates.

We use an EnKF variant known as the ensemble square root Kalman filter (EnSRF; Andrews 1968), which removes the need for perturbed observations (Whitaker and Hamill 2002). Consequently,  $\mathbf{Y}$  is a matrix with constant rows. In the EnSRF formulation, ensemble deviations are updated separately from the mean, as per:

$$\bar{\mathbf{x}}_a = \bar{\mathbf{x}}_p + \mathbf{K}(\bar{\mathbf{y}} - \bar{\mathbf{y}}_e) \quad (\text{A2})$$

$$\mathbf{X}'_a = \mathbf{X}'_p - \tilde{\mathbf{K}}\mathbf{Y}'_e \quad (\text{A3})$$

657 where an overbar ( $\bar{\mathbf{x}}$ ) denotes an ensemble average, and a tick ( $\mathbf{X}'$ ) indicates deviations from an  
 658 ensemble mean. Here, the ensemble mean is updated via the Kalman gain ( $\mathbf{K}$ ):

$$\mathbf{K} = \text{cov}(\mathbf{X}_p, \mathbf{Y}_e) \times [\text{cov}(\mathbf{Y}_e, \mathbf{Y}_e) + \mathbf{R}]^{-1} \quad (\text{A4})$$

659 and the deviations are updated via an adjusted gain ( $\tilde{\mathbf{K}}$ ):

$$\tilde{\mathbf{K}} = \text{cov}(\mathbf{X}_p, \mathbf{Y}_e) \times [(\sqrt{\text{cov}(\mathbf{Y}_e, \mathbf{Y}_e) + \mathbf{R}})^{-1}]^T [\sqrt{\text{cov}(\mathbf{Y}_e, \mathbf{Y}_e) + \mathbf{R}} + \sqrt{\mathbf{R}}]^{-1} \quad (\text{A5})$$

660 Here,  $\mathbf{R}$  denotes the observation error-covariance matrix ( $d \times d$ ). We do not consider correlated  
 661 measurement errors in this study, so  $\mathbf{R}$  is a diagonal matrix whose elements are the observation  
 662 uncertainties determined from the variances of the residuals for the forward model regressions.

## 663 A2. Covariance Localization

664 We implement a covariance localization scheme, modifying the Kalman Gain equations to:

$$\mathbf{K} = \mathbf{W}_{\text{loc}} \circ \text{cov}(\mathbf{X}_p, \mathbf{Y}_e) \times [\mathbf{Y}_{\text{loc}} \circ \text{cov}(\mathbf{Y}_e, \mathbf{Y}_e) + \mathbf{R}]^{-1} \quad (\text{A6})$$

665 and

$$\tilde{\mathbf{K}} = \mathbf{W}_{\text{loc}} \circ \text{cov}(\mathbf{X}_p, \mathbf{Y}_e) \times [(\sqrt{\mathbf{Y}_{\text{loc}} \circ \text{cov}(\mathbf{Y}_e, \mathbf{Y}_e) + \mathbf{R}})^{-1}]^T [\sqrt{\mathbf{Y}_{\text{loc}} \circ \text{cov}(\mathbf{Y}_e, \mathbf{Y}_e) + \mathbf{R}} + \sqrt{\mathbf{R}}]^{-1}. \quad (\text{A7})$$

666 Here,  $\mathbf{W}_{\text{loc}}$  ( $n \times d$ ) and  $\mathbf{Y}_{\text{loc}}$  ( $d \times d$ ) are matrices of covariance localization weights applied to  
 667 the covariance of proxy sites with model grid cells ( $\mathbf{W}_{\text{loc}}$ ) and proxy sites with one another ( $\mathbf{Y}_{\text{loc}}$ ).

668 We implement localization weights as a fifth order Gaspari-Cohn polynomial (Gaspari and Cohn

1999) applied to the distance between proxy sites and model grid cells ( $\mathbf{W}_{loc}$ ) or proxy sites with one another ( $\mathbf{Y}_{loc}$ ). Weights are applied to covariance matrices via element-wise multiplication.

The localization radius is an important free parameter that must be assessed independently for different model priors, reconstruction targets, and proxy networks. Here, we select localization radii using a two step process. For a given model prior and target field, we first assimilate the proxy network from 1901-1988 CE using each localization radius from 250 km to 50,000 km in steps of 250 km and a run with no localization. We then determine the  $\sigma$  ratio of each reconstructed extratropical MJJA time series in a calibration interval. We find the  $\sigma$  ratio closest to 1 and record the associated localization radius as “optimal”. We then calculate skill metrics for the extratropical MJJA time series over a validation interval using the reconstruction with the optimal radius.

To limit the sensitivity of this method to the calibration period (Christiansen et al. 2009), we perform this optimization using each set of 44 contiguous years from 1901-1988 CE once as a calibration interval and once as a validation interval. The final localization radius is the median of the 88 “optimal” radii, and the median validation skill metrics are reported.

#### *a. Selection Criterion*

In the development of this method, we tested an RMSE selection criterion in addition to  $\sigma$  ratios. We find that correlation coefficients, RMSE values, and mean biases of the reconstructed mean extratropical MJJA time series are all insensitive to the choice of selection criteria (Table 2, Table A1), but that  $\sigma$  ratios are more sensitive. Specifically, mean  $\sigma$  ratios are near 0.8 for the RMSE selection criterion, but rise to 1.11 for the  $\sigma$  ratio scheme. Since the  $\sigma$  ratio localization selection criteria brings the  $\sigma$  ratio skill metric closer to 1 without appreciably altering the other skill metrics, and because of the tendency for our DA method to underestimate temporal variability, we use a  $\sigma$  ratio selection criterion.

## 692 **References**

- 693 Acevedo, W., B. Fallah, S. Reich, and U. Cubasch, 2017: Assimilation of pseudo-tree-ring-width  
694 observations into an atmospheric general circulation model. *Climate of the Past*, **13 (5)**, 545–557.
- 695 Ammann, C., 2008: The paleoclimate reconstruction challenge. *PAGES News*, **16 (1)**, 4.
- 696 Ammann, C. M., and E. R. Wahl, 2007: The importance of the geophysical context in statistical  
697 evaluations of climate reconstruction procedures. *Climatic Change*, **85 (1)**, 71–88.
- 698 Anchukaitis, K. J., and N. McKay, 2015: PAGES2k: Advances in climate field reconstructions.  
699 *PAGES Magazine*, **22 (2)**, 98.
- 700 Anchukaitis, K. J., and Coauthors, 2017: Last millennium Northern Hemisphere summer temper-  
701 atures from tree rings: Part II, spatially resolved reconstructions. *Quaternary Science Reviews*,  
702 **163**, 1–22.
- 703 Andrews, A., 1968: A square root formulation of the Kalman covariance equations. *AIAA Journal*,  
704 **6 (6)**, 1165–1166.
- 705 Annan, J., and J. Hargreaves, 2012: Identification of climatic state with limited proxy data. *Climate*  
706 *of the Past*, **8 (4)**, 1141–1151.
- 707 Bhend, J., J. Franke, D. Folini, M. Wild, and S. Brönnimann, 2012: An ensemble-based approach  
708 to climate reconstructions. *Climate of the Past*, **8 (3)**, 963–976.
- 709 Björklund, J., B. E. Gunnarson, K. Seftigen, J. Esper, and Coauthors, 2014: Blue intensity and  
710 density from northern fennoscandian tree rings, exploring the potential to improve summer  
711 temperature reconstructions with earlywood information. *Climate of the Past*, **10 (2)**, 877–885.

- 712 Böhm, R., P. D. Jones, J. Hiebl, D. Frank, M. Brunetti, and M. Maugeri, 2010: The early  
713 instrumental warm-bias: a solution for long central european temperature series 1760–2007.  
714 *Climatic Change*, **101 (1-2)**, 41–67.
- 715 Chen, Z., and Coauthors, 2003: Bayesian filtering: From Kalman filters to particle filters, and  
716 beyond. *Statistics*, **182 (1)**, 1–69.
- 717 Christiansen, B., 2008: Volcanic eruptions, large-scale modes in the northern hemisphere, and the  
718 el niño–southern oscillation. *Journal of Climate*, **21 (5)**, 910–922.
- 719 Christiansen, B., and F. C. Ljungqvist, 2017: Challenges and perspectives for large-scale temper-  
720 ature reconstructions of the past two millennia. *Reviews of Geophysics*, **55 (1)**, 40–96.
- 721 Christiansen, B., T. Schmith, and P. Thejll, 2009: A surrogate ensemble study of climate recon-  
722 struction methods: Stochasticity and robustness. *Journal of Climate*, **22 (4)**, 951–976.
- 723 Comboul, M., J. Emile-Geay, G. J. Hakim, and M. N. Evans, 2015: Paleoclimate sampling as a  
724 sensor placement problem. *Journal of Climate*, **28**, 7717–7740, doi:10.1175/JCLI-D-14-00802.  
725 1.
- 726 Cook, E. R., K. J. Anchukaitis, B. M. Buckley, R. D. D’Arrigo, G. C. Jacoby, and W. E. Wright,  
727 2010a: Asian monsoon failure and megadrought during the last millennium. *Science*, **328 (5977)**,  
728 486–489.
- 729 Cook, E. R., K. R. Briffa, and P. D. Jones, 1994: Spatial regression methods in dendroclimatology:  
730 a review and comparison of two techniques. *International Journal of Climatology*, **14 (4)**,  
731 379–402.

- 732 Cook, E. R., P. J. Krusic, K. J. Anchukaitis, B. M. Buckley, T. Nakatsuka, M. Sano, and Coauthors,  
733 2013: Tree-ring reconstructed summer temperature anomalies for temperate East Asia since 800  
734 CE. *Climate Dynamics*, **41 (11-12)**, 2957–2972.
- 735 Cook, E. R., D. M. Meko, D. W. Stahle, and M. K. Cleaveland, 1999: Drought reconstructions for  
736 the continental United States. *Journal of Climate*, **12 (4)**, 1145–1162.
- 737 Cook, E. R., R. Seager, R. R. Heim Jr, R. S. Vose, C. Herweijer, and C. Woodhouse, 2010b:  
738 Megadroughts in North America: Placing IPCC projections of hydroclimatic change in a long-  
739 term palaeoclimate context. *Journal of Quaternary Science*, **25 (1)**, 48–61.
- 740 Cort, G. D., M. Chevalier, S. L. Burrough, C. Y. Chen, and S. P. Harrison, 2021: An uncertainty-  
741 focused database approach to extract spatiotemporal trends from qualitative and discontinuous  
742 lake-status histories. *Quaternary Science Reviews*, **258**, 106 870, doi:10.1016/j.quascirev.2021.  
743 106870, URL <https://doi.org/10.1016/j.quascirev.2021.106870>.
- 744 Cowtan, K., and R. G. Way, 2014: Coverage bias in the HadCRUT4 temperature series and its  
745 impact on recent temperature trends. *Quarterly Journal of the Royal Meteorological Society*,  
746 **140 (683)**, 1935–1944.
- 747 De Silva, S. L., and G. A. Zielinski, 1998: Global influence of the AD 1600 eruption of Huayna-  
748 putina, Peru. *Nature*, **393 (6684)**, 455–458.
- 749 Dee, S. G., N. J. Steiger, J. Emile-Geay, and G. J. Hakim, 2016: On the utility of proxy system  
750 models for estimating climate states over the Common Era. *Journal of Advances in Modeling  
751 Earth Systems*, **8 (3)**, 1164–1179.
- 752 Delworth, T. L., and M. E. Mann, 2000: Observed and simulated multidecadal variability in the  
753 Northern Hemisphere. *Climate Dynamics*, **16 (9)**, 661–676.

- 754 Dubinkina, S., and H. Goosse, 2013: An assessment of particle filtering methods and nudging for  
755 climate state reconstructions. *Climate of the Past*, **9** (3), 1141–1152.
- 756 Esper, J., D. C. Frank, R. J. Wilson, and K. R. Briffa, 2005: Effect of scaling and regression  
757 on reconstructed temperature amplitude for the past millennium. *Geophysical Research Letters*,  
758 **32** (7).
- 759 Esper, J., and Coauthors, 2018: Large-scale, millennial-length temperature reconstructions from  
760 tree-rings. *Dendrochronologia*, **50**, 81–90, doi:10.1016/j.dendro.2018.06.001.
- 761 Evans, M., A. Kaplan, M. Cane, and R. Villalba, 2001: Globality and optimality in climate field  
762 reconstructions from proxy data. *Interhemispheric Climate Linkages*, Elsevier, 53–XV.
- 763 Evans, M. N., A. Kaplan, and M. A. Cane, 2002: Pacific sea surface temperature field reconstruction  
764 from coral  $\delta^{18}\text{O}$  data using reduced space objective analysis. *Paleoceanography*, **17** (1), doi:  
765 10.1029/2000PA000590.
- 766 Evans, M. N., S. E. Tolwinski-Ward, D. M. Thompson, and K. J. Anchukaitis, 2013: Applications  
767 of proxy system modeling in high resolution paleoclimatology. *Quaternary Science Reviews*,  
768 **76**, 16–28.
- 769 Evensen, G., 1994: Sequential data assimilation with a nonlinear quasi-geostrophic model using  
770 Monte Carlo methods to forecast error statistics. *Journal of Geophysical Research: Oceans*,  
771 **99** (C5), 10 143–10 162.
- 772 Evensen, G., 2003: The ensemble Kalman filter: Theoretical formulation and practical implemen-  
773 tation. *Ocean Dynamics*, **53** (4), 343–367.

- 774 Frank, D., U. Büntgen, R. Böhm, M. Maugeri, and J. Esper, 2007: Warmer early instrumental mea-  
775 surements versus colder reconstructed temperatures: shooting at a moving target. *Quaternary*  
776 *Science Reviews*, **26 (25-28)**, 3298–3310.
- 777 Frank, D., J. Esper, E. Zorita, and R. Wilson, 2010: A noodle, hockey stick, and spaghetti plate:  
778 a perspective on high-resolution paleoclimatology. *Wiley Interdisciplinary Reviews: Climate*  
779 *Change*, **1 (4)**, 507–516.
- 780 Franke, J., V. Valler, S. Brönnimann, R. Neukom, and F. Jaume-Santero, 2020: The impor-  
781 tance of input data quality and quantity in climate field reconstructions – results from the  
782 assimilation of various tree-ring collections. *Climate of the Past*, **16 (3)**, 1061–1074, doi:  
783 10.5194/cp-16-1061-2020.
- 784 Fritts, H. C., 1991: *Reconstructing large-scale climatic patterns from tree-ring data: a diagnostic*  
785 *analysis*. University of Arizona Press.
- 786 Gaspari, G., and S. E. Cohn, 1999: Construction of correlation functions in two and three dimen-  
787 sions. *Quarterly Journal of the Royal Meteorological Society*, **125 (554)**, 723–757.
- 788 Gennaretti, F., D. Arseneault, A. Nicault, L. Perreault, and Y. Bégin, 2014: Volcano-induced regime  
789 shifts in millennial tree-ring chronologies from northeastern North America. *Proceedings of the*  
790 *National Academy of Sciences*, **111 (28)**, 10 077–10 082.
- 791 Gill, E. C., B. Rajagopalan, P. Molnar, and T. M. Marchitto, 2016: Reduced-dimension reconstruc-  
792 tion of the equatorial pacific sst and zonal wind fields over the past 10,000 years using mg/ca  
793 and alkenone records. *Paleoceanography*, **31 (7)**, 928–952.

- 794 Goosse, H., 2016: An additional step toward comprehensive paleoclimate reanalyses. *Journal of*  
795 *Advances in Modeling Earth Systems*, n/a–n/a, doi:10.1002/2016MS000739, URL [http://dx.doi.](http://dx.doi.org/10.1002/2016MS000739)  
796 [org/10.1002/2016MS000739](http://dx.doi.org/10.1002/2016MS000739).
- 797 Goosse, H., 2017: Reconstructed and simulated temperature asymmetry between continents in  
798 both hemispheres over the last centuries. *Climate Dynamics*, **48 (5-6)**, 1483–1501.
- 799 Goosse, H., J. Guiot, M. E. Mann, S. Dubinkina, and Y. Sallaz-Damaz, 2012: The Medieval  
800 Climate Anomaly in Europe: Comparison of the summer and annual mean signals in two  
801 reconstructions and in simulations with data assimilation. *Global and Planetary Change*, **84**,  
802 35–47.
- 803 Graham, N., and E. Wahl, 2011: Paleoclimate reconstruction challenge. *PAGES/CLIVAR Newslet-*  
804 *ter*, **19 (2)**, 71–72.
- 805 Guillet, S., and Coauthors, 2017: Climate response to the Samalas volcanic eruption in 1257  
806 revealed by proxy records. *Nature Geoscience*, **10 (2)**, 123–128.
- 807 Guillot, D., B. Rajaratnam, and J. Emile-Geay, 2015: Statistical paleoclimate reconstructions via  
808 Markov random fields. *The Annals of Applied Statistics*, **9 (1)**, 324–352.
- 809 Hakim, G. J., J. Emile-Geay, E. J. Steig, D. Noone, D. M. Anderson, R. Tardif, N. Steiger, and  
810 W. A. Perkins, 2016: The Last Millennium Climate Reanalysis project: Framework and first  
811 results. *Journal of Geophysical Research: Atmospheres*, **121 (12)**, 6745–6764.
- 812 Harris, I., P. D. Jones, T. J. Osborn, and D. H. Lister, 2014: Updated high-resolution grids of  
813 monthly climatic observations—the CRU TS3.10 Dataset. *International Journal of Climatology*,  
814 **34 (3)**, 623–642.

- 815 Haurwitz, M. W., and G. W. Brier, 1981: A critique of the superposed epoch analysis method: its  
816 application to solar–weather relations. *Monthly Weather Review*, **109** (10), 2074–2079.
- 817 Hegerl, G., and P. Stott, 2014: From past to future warming. *Science*, **343** (6173), 844–845.
- 818 Hegerl, G. C., T. J. Crowley, M. Allen, W. T. Hyde, H. N. Pollack, J. Smerdon, and E. Zorita,  
819 2007: Detection of human influence on a new, validated 1500-year temperature reconstruction.  
820 *Journal of Climate*, **20** (4), 650–666.
- 821 Hegerl, G. C., T. J. Crowley, S. K. Baum, K.-Y. Kim, and W. T. Hyde, 2003: Detection of volcanic,  
822 solar and greenhouse gas signals in paleo-reconstructions of Northern Hemispheric temperature.  
823 *Geophysical Research Letters*, **30** (5), doi:10.1029/2002GL016635.
- 824 Hegerl, G. C., K. Hasselmann, U. Cubasch, J. F. Mitchell, E. Roeckner, R. Voss, and J. Waszkewitz,  
825 1997: Multi-fingerprint detection and attribution analysis of greenhouse gas, greenhouse gas-  
826 plus-aerosol and solar forced climate change. *Climate Dynamics*, **13** (9), 613–634.
- 827 Houtekamer, P. L., and H. L. Mitchell, 2001: A sequential ensemble Kalman filter for atmospheric  
828 data assimilation. *Monthly Weather Review*, **129** (1), 123–137.
- 829 Hughes, M., and C. Ammann, 2009: The future of the past—an earth system framework for high  
830 resolution paleoclimatology: editorial essay. *Climatic Change*, **94** (3-4), 247–259.
- 831 Kaufman, D., 2014: A community-driven framework for climate reconstructions. *Eos, Transactions*  
832 *American Geophysical Union*, **95** (40), 361–362, doi:10.1002/2014eo400001.
- 833 Lavigne, F., and Coauthors, 2013: Source of the great AD 1257 mystery eruption unveiled,  
834 Samalas volcano, Rinjani Volcanic Complex, Indonesia. *Proceedings of the National Academy*  
835 *of Sciences*, **110** (42), 16 742–16 747.

- 836 Lean, J. L., and D. H. Rind, 2008: How natural and anthropogenic influences alter global and  
837 regional surface temperatures: 1889 to 2006. *Geophysical Research Letters*, **35 (18)**, doi:  
838 10.1029/2008GL034864.
- 839 Liu, H., Z. Liu, and F. Lu, 2017: A systematic comparison of particle filter and EnKF in assimilating  
840 time-averaged observations. *Journal of Geophysical Research: Atmospheres*, **122 (24)**, 13–155.
- 841 Mann, M. E., R. S. Bradley, and M. K. Hughes, 1998: Global-scale temperature patterns and  
842 climate forcing over the past six centuries. *Nature*, **392 (6678)**, 779–787.
- 843 Mann, M. E., and S. Rutherford, 2002: Climate reconstruction using ‘Pseudoproxies’. *Geophysical*  
844 *Research Letters*, **29 (10)**, 139–1.
- 845 Mann, M. E., and Coauthors, 2009: Global signatures and dynamical origins of the Little Ice Age  
846 and Medieval Climate Anomaly. *Science*, **326 (5957)**, 1256–1260.
- 847 Marsland, S. J., H. Haak, J. H. Jungclaus, M. Latif, and F. Röske, 2003: The Max-Planck-Institute  
848 global ocean/sea ice model with orthogonal curvilinear coordinates. *Ocean Modelling*, **5 (2)**,  
849 91–127.
- 850 Masson-Delmotte, V., and Coauthors, 2013: Information from Paleoclimate Archives. *Climate*  
851 *Change 2013: The Physical Science Basis. Contribution of Working Group I to the Fifth*  
852 *Assessment Report of the Intergovernmental Panel on Climate Change*, T. F. Stocker, D. Qin,  
853 G.-K. Plattner, M. Tignor, S. Allen, J. Boschung, A. Nauels, Y. Xia, V. Bex, and P. Midgley, Eds.,  
854 Cambridge University Press, Cambridge, United Kingdom and New York, NY, USA, 383–464.
- 855 Matsikaris, A., M. Widmann, and J. H. Jungclaus, 2015: On-line and off-line data assimilation in  
856 palaeoclimatology: a case study. *Climate of the Past*, **11**, 81–93.

- 857 McCarroll, D., E. Pettigrew, A. Luckman, F. Guibal, and J.-L. Edouard, 2002: Blue reflectance  
858 provides a surrogate for latewood density of high-latitude pine tree rings. *Arctic, Antarctic, and*  
859 *Alpine Research*, **34 (4)**, 450–453.
- 860 Meehl, G. A., W. M. Washington, C. M. Ammann, J. M. Arblaster, T. Wigley, and C. Tebaldi, 2004:  
861 Combinations of natural and anthropogenic forcings in twentieth-century climate. *Journal of*  
862 *Climate*, **17 (19)**, 3721–3727.
- 863 Meko, D., 1997: Dendroclimatic reconstruction with time varying predictor subsets of tree indices.  
864 *Journal of Climate*, **10**, 687–696.
- 865 Neukom, R., N. Steiger, J. J. Gómez-Navarro, J. Wang, and J. P. Werner, 2019: No evidence for  
866 globally coherent warm and cold periods over the preindustrial Common Era. *Nature*, **571 (7766)**,  
867 550–554.
- 868 Okazaki, A., and K. Yoshimura, 2017: Development and evaluation of a system of proxy data  
869 assimilation for paleoclimate reconstruction. *Climate of the Past*, **13 (4)**, 379–393.
- 870 Oke, P. R., J. S. Allen, R. N. Miller, G. D. Egbert, and P. M. Kosro, 2002: Assimilation of surface  
871 velocity data into a primitive equation coastal ocean model. *Journal of Geophysical Research:*  
872 *Oceans*, **107 (C9)**, doi:10.1029/2000JC000511.
- 873 Otto-Bliesner, B. L., and Coauthors, 2016: Climate variability and change since 850 CE: An ensem-  
874 ble approach with the Community Earth System Model. *Bulletin of the American Meteorological*  
875 *Society*, **97 (5)**, 735–754.
- 876 PAGES2k Consortium, 2013: Continental-scale temperature variability during the past two mil-  
877 lennia. *Nature Geoscience*, **6 (5)**, 339–346.

878 PAGES2k Consortium, 2017: A global multiproxy database for temperature reconstructions of the  
879 Common Era. *Scientific Data*, **4**, 170 088.

880 Parker, D., 1994: Effects of changing exposure of thermometers at land stations. *International*  
881 *Journal of Climatology*, **14 (1)**, 1–31.

882 Perkins, W. A., and G. J. Hakim, 2017: Reconstructing paleoclimate fields using online data  
883 assimilation with a linear inverse model. *Climate of the Past*, **13 (5)**, 421–436.

884 Phipps, S. J., and Coauthors, 2013: Paleoclimate data–model comparison and the role of climate  
885 forcings over the past 1500 years. *Journal of Climate*, **26 (18)**, 6915–6936.

886 Robock, A., 2000: Volcanic eruptions and climate. *Reviews of geophysics*, **38 (2)**, 191–219.

887 Rohde, R., and Coauthors, 2013: Berkeley Earth temperature averaging process. *Geoinformatics*  
888 *and Geostatistics: An Overview*, **1 (2)**, 20–100.

889 Rutherford, S., M. Mann, T. Delworth, and R. Stouffer, 2003: Climate field reconstruction under  
890 stationary and nonstationary forcing. *Journal of Climate*, **16 (3)**, 462–479.

891 Rydval, M., L.-Å. Larsson, L. McGlynn, B. E. Gunnarson, N. J. Loader, G. H. Young, and  
892 R. Wilson, 2014: Blue intensity for dendroclimatology: should we have the blues? Experiments  
893 from Scotland. *Dendrochronologia*, **32 (3)**, 191–204.

894 Schneider, D. P., C. M. Ammann, B. L. Otto-Bliesner, and D. S. Kaufman, 2009: Climate response  
895 to large, high-latitude and low-latitude volcanic eruptions in the Community Climate System  
896 Model. *Journal of Geophysical Research: Atmospheres*, **114 (D15)**.

897 Schneider, T., 2001: Analysis of incomplete climate data: Estimation of mean values and covari-  
898 ance matrices and imputation of missing values. *Journal of Climate*, **14 (5)**, 853–871.

- 899 Schurer, A. P., G. C. Hegerl, M. E. Mann, S. F. B. Tett, and S. J. Phipps, 2013: Separating  
900 forced from chaotic climate variability over the past millennium. *Journal of Climate*, **26** (18),  
901 6954–6973, doi:10.1175/jcli-d-12-00826.1.
- 902 Schweingruber, F., H. Fritts, O. Bräker, L. Drew, and E. Schär, 1978: The x-ray technique as  
903 applied to dendroclimatology. *Tree-Ring Bulletin*, **38**, 61–91.
- 904 Seager, R., N. Graham, C. Herweijer, A. L. Gordon, Y. Kushnir, and E. Cook, 2007: Blueprints  
905 for medieval hydroclimate. *Quaternary Science Reviews*, **26** (19-21), 2322–2336.
- 906 Sigl, M., and Coauthors, 2015: Timing and climate forcing of volcanic eruptions for the past 2,500  
907 years. *Nature*, **523** (7562), 543–549.
- 908 Smerdon, J. E., 2012: Climate models as a test bed for climate reconstruction methods: pseudo-  
909 proxy experiments. *Wiley Interdisciplinary Reviews: Climate Change*, **3** (1), 63–77.
- 910 Smerdon, J. E., A. Kaplan, E. Zorita, J. F. González-Rouco, and M. Evans, 2011: Spatial per-  
911 formance of four climate field reconstruction methods targeting the Common Era. *Geophysical*  
912 *Research Letters*, **38** (11), doi:10.1029/2011GL047372.
- 913 Smerdon, J. E., and H. N. Pollack, 2016: Reconstructing Earth’s surface temperature over the past  
914 2000 years: the science behind the headlines. *Wiley Interdisciplinary Reviews: Climate Change*,  
915 **7** (5), 746–771.
- 916 Solomon, A., and Coauthors, 2011: Distinguishing the roles of natural and anthropogenically forced  
917 decadal climate variability: implications for prediction. *Bulletin of the American Meteorological*  
918 *Society*, **92** (2), 141–156.
- 919 Steiger, N. J., G. J. Hakim, E. J. Steig, D. S. Battisti, and G. H. Roe, 2014: Assimilation of  
920 time-averaged pseudoproxies for climate reconstruction. *Journal of Climate*, **27** (1), 426–441.

- 921 Steiger, N. J., and J. E. Smerdon, 2017: A pseudoproxy assessment of data assimilation for  
922 reconstructing the atmosphere–ocean dynamics of hydroclimate extremes. *Climate of the Past*,  
923 **13 (10)**, 1435–1449.
- 924 Steiger, N. J., J. E. Smerdon, E. R. Cook, and B. I. Cook, 2018: A reconstruction of global  
925 hydroclimate and dynamical variables over the common era. *Scientific Data*, **5**, doi:10.1086/  
926 sdata.2018.86.
- 927 Stenchikov, G., K. Hamilton, R. J. Stouffer, A. Robock, V. Ramaswamy, B. Santer, and H.-F.  
928 Graf, 2006: Arctic Oscillation response to volcanic eruptions in the IPCC AR4 climate models.  
929 *Journal of Geophysical Research: Atmospheres*, **111 (D7)**.
- 930 Stevens, B., and Coauthors, 2013: Atmospheric component of the MPI-M earth system model:  
931 ECHAM6. *Journal of Advances in Modeling Earth Systems*, **5 (2)**, 146–172.
- 932 Stott, P. A., N. P. Gillett, G. C. Hegerl, D. J. Karoly, D. A. Stone, X. Zhang, and F. Zwiers, 2010:  
933 Detection and attribution of climate change: a regional perspective. *Wiley Interdisciplinary*  
934 *Reviews: Climate Change*, **1 (2)**, 192–211.
- 935 Stott, P. A., and G. S. Jones, 2009: Variability of high latitude amplification of anthropogenic  
936 warming. *Geophysical Research Letters*, **36 (10)**, doi:10.1029/2009GL037698.
- 937 Stott, P. A., and S. F. Tett, 1998: Scale-dependent detection of climate change. *Journal of Climate*,  
938 **11 (12)**, 3282–3294.
- 939 Sundqvist, H. S., and Coauthors, 2014: Arctic Holocene proxy climate database–new approaches  
940 to assessing geochronological accuracy and encoding climate variables. *Climate of the Past*, **10**,  
941 1605–1631, doi:10.5194/cp-10-1605-2014.

- 942 Tardif, R., and Coauthors, 2019: Last Millennium Reanalysis with an expanded proxy database  
943 and seasonal proxy modeling. *Climate of the Past*, **15** (4), 1251–1273.
- 944 Taylor, K. E., R. J. Stouffer, and G. A. Meehl, 2012: An overview of CMIP5 and the experiment  
945 design. *Bulletin of the American Meteorological Society*, **93** (4), 485–498.
- 946 Tingley, M. P., P. F. Craigmile, M. Haran, B. Li, E. Mannshardt, and B. Rajaratnam, 2012: Piecing  
947 together the past: Statistical insights into paleoclimatic reconstructions. *Quaternary Science*  
948 *Reviews*, **35**, 1–22.
- 949 Valler, V., J. Franke, and S. Brönnimann, 2019: Impact of different estimations of the background-  
950 error covariance matrix on climate reconstructions based on data assimilation. *Climate of the*  
951 *Past*, **15** (4), 1427–1441, doi:10.5194/cp-15-1427-2019.
- 952 Van der Schrier, G., and J. Barkmeijer, 2005: Bjerknes’ hypothesis on the coldness during AD  
953 1790–1820 revisited. *Climate Dynamics*, **25** (5), 537–553.
- 954 Wang, J., J. Emile-Geay, D. Guillot, N. P. McKay, and B. Rajaratnam, 2015: Fragility of re-  
955 constructed temperature patterns over the common era: Implications for model evaluation.  
956 *Geophysical Research Letters*, **42** (17), 7162–7170.
- 957 Wang, J., J. Emile-Geay, D. Guillot, J. E. Smerdon, and B. Rajaratnam, 2014: Evaluating climate  
958 field reconstruction techniques using improved emulations of real-world conditions. *Climate of*  
959 *the Past*, **10** (1), 1–19, doi:10.5194/cp-10-1-2014.
- 960 Whitaker, J. S., and T. M. Hamill, 2002: Ensemble data assimilation without perturbed observa-  
961 tions. *Monthly Weather Review*, **130** (7), 1913–1924.

- 962 Widmann, M., H. Goosse, G. van der Schrier, R. Schnur, and J. Barkmeijer, 2010: Using data  
963 assimilation to study extratropical northern hemisphere climate over the last millennium. *Climate*  
964 *of the Past*, **6 (5)**, 627–644, doi:10.5194/cp-6-627-2010.
- 965 Wikle, C. K., and L. M. Berliner, 2007: A Bayesian tutorial for data assimilation. *Physica D:*  
966 *Nonlinear Phenomena*, **230 (1-2)**, 1–16.
- 967 Wilson, R., and Coauthors, 2016: Last millennium northern hemisphere summer temperatures  
968 from tree rings: Part I: The long term context. *Quaternary Science Reviews*, **134**, 1–18.
- 969 Wilson, R., and Coauthors, 2019: Improved dendroclimatic calibration using blue intensity in the  
970 southern Yukon. *The Holocene*, **29 (11)**, 1817–1830.
- 971 Zhu, F., J. Emile-Geay, G. J. Hakim, J. King, and K. J. Anchukaitis, 2020: Resolving the differences  
972 in the simulated and reconstructed temperature response to volcanism. *Geophysical Research*  
973 *Letters*, **47 (8)**, e2019GL086908.
- 974 Zorita, E., F. González-Rouco, and S. Legutke, 2003: Testing the approach to paleoclimate  
975 reconstructions in the context of a 1000-yr control simulation with the ECHO-G coupled climate  
976 model. *Journal of Climate*, **16 (9)**, 1378–1390.

977 **LIST OF TABLES**

978 **Table 1.** Summary of climate models used to construct data assimilation prior ensembles.  
 979 Climate models are listed along with the identifying acronym used in this study.  
 980 The years of available output are provided with the experiment used to generate  
 981 them. The size of the model prior generated from these years is also provided.  
 982 Taylor et al. (2012) provide more details on the PMIP3 and CMIP5 experiments,  
 983 and Otto-Bliesner et al. (2016) describe the LME. . . . . 48

984 **Table 2.** Calibrated localization radii. Localization radii for individual model priors are  
 985 selected using the radius search and calibration-validation procedure detailed  
 986 in Appendix A1. Skill metrics are the median values obtained for the mean  
 987 extratropical MJJA time series relative to BEST for the set of validation periods. . . . 49

988 **Table 3.** Temperature field reconstructions used to compare spatial patterns of climate  
 989 response to radiative forcings in this study. We provide a reference for each  
 990 CFR along with the name used in this study. We also note the maximum size  
 991 of the proxy network used in each study along with the target temperature fields. . . . 50

992 **Table 4.** Withheld proxy verification statistics for individual models. Reported skill  
 993 metrics are the median for all individual proxy comparisons over the 54 leave-  
 994 one-out assimilations. . . . . 51

995 **Table A1.** As in Table 2, but using the RMSE optimization scheme. . . . . 52

996 TABLE 1. Summary of climate models used to construct data assimilation prior ensembles. Climate models  
997 are listed along with the identifying acronym used in this study. The years of available output are provided with  
998 the experiment used to generate them. The size of the model prior generated from these years is also provided.  
999 Taylor et al. (2012) provide more details on the PMIP3 and CMIP5 experiments, and Otto-Bliesner et al. (2016)  
1000 describe the LME.

Model	Acronym	Years: Experiment	Sample size ( $m$ )
BCC-CSM1-1	BCC	850-2000: past1000	1151
CCSM4	CCSM4	850-1850: past1000 1851-2005: historical	1156
CESM1.1-CAM5	CESM	850-2005: LME full-forcing	1156
CSIRO-Mk3L-1-2	CSIRO	851-1850: past1000 1851-2000: historical	1150
FGOALS-g1	FGOALS	1000-1999: past1000	1000
HadCM3	HadCM3	850-1850: past1000 1859-2000: historical	1147
IPSL-CM5A-LR	IPSL	850-1850: past1000 1851-2005: historical	1156
MIROC-ESM	MIROC	850-1849: past1000 1850-2005: historical	1156
MPI-ESM-P	MPI	850-1849: past1000 1850-2005: historical	1156
MRI-CGCM3	MRI	850-1850: past1000 1850-2005: historical	1156

1001 TABLE 2. Calibrated localization radii. Localization radii for individual model priors are selected using the  
 1002 radius search and calibration-validation procedure detailed in Appendix A1. Skill metrics are the median values  
 1003 obtained for the mean extratropical MJJA time series relative to BEST for the set of validation periods.

Model	Localization Radius (km)	Correlation	RMSE (°C)	$\sigma$ Ratio	Mean Bias (°C)
BCC	$\infty$	0.69	0.18	1.03	0.05
CCSM4	16500	0.72	0.19	1.18	0.07
CESM	$\infty$	0.72	0.18	1.08	0.06
CSIRO	$\infty$	0.70	0.19	1.18	0.05
F-GOALS	$\infty$	0.70	0.18	1.02	0.07
HadCM3	$\infty$	0.69	0.19	1.18	0.05
IPSL	12750	0.70	0.19	1.19	0.06
MIROC	26375	0.71	0.19	1.18	0.06
MPI	27625	0.69	0.20	1.18	0.06
MRI	$\infty$	0.71	0.17	1.01	0.05

1004 TABLE 3. Temperature field reconstructions used to compare spatial patterns of climate response to radiative  
 1005 forcings in this study. We provide a reference for each CFR along with the name used in this study. We also note  
 1006 the maximum size of the proxy network used in each study along with the target temperature fields.

Name	Reference	Network Size	Reconstruction Target
NTREND - DA	This study	54	MJJA
NTREND - PPR	Anchukaitis et al. (2017)	54	MJJA
Guillet 2017	Guillet et al. (2017)	28	Highpass JJA
Zhu 2020	Zhu et al. (2020)	395	JJA
LMR 2.1	Tardif et al. (2019)	544	Annual (Jan. - Dec.)
Neukom (DA)	Neukom et al. (2019)	210	Annual (April - March)

1007 TABLE 4. Withheld proxy verification statistics for individual models. Reported skill metrics are the median  
 1008 for all individual proxy comparisons over the 54 leave-one-out assimilations.

Model	Correlation	RMSE	$\sigma$ Ratio	Mean Bias °C
BCC	0.53	0.98	0.42	0.12
CCSM4	0.52	0.98	0.42	0.06
CESM	0.50	1.03	0.35	0.27
CSIRO	0.54	1.01	0.31	0.13
F-GOALS	0.47	1.04	0.34	0.06
HadCM3	0.49	1.03	0.39	0.25
IPSL	0.53	1.00	0.38	0.08
MIROC	0.53	1.01	0.37	0.25
MPI	0.53	0.99	0.39	0.11
MRI	0.55	0.98	0.32	0.16

Table A1. As in Table 2, but using the RMSE optimization scheme.

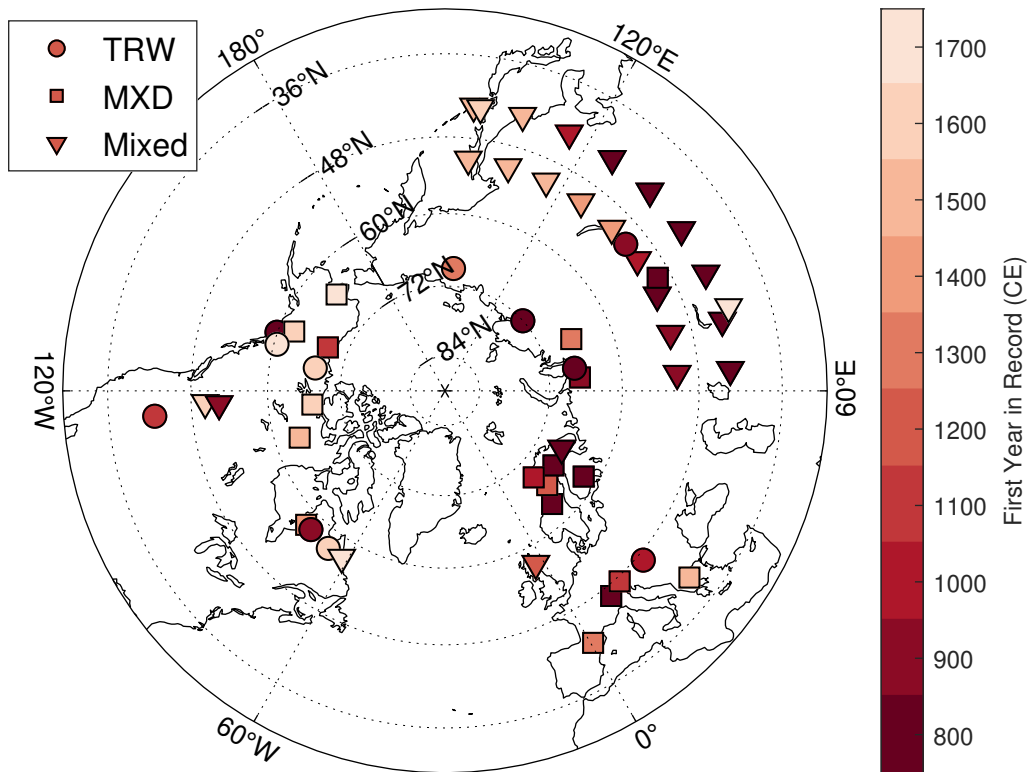
Model	Localization Radius (km)	Correlation	RMSE (°C)	$\sigma$ Ratio	Mean Bias (°C)
BCC	18875	0.71	0.17	0.78	0.06
CCSM4	7375	0.71	0.18	0.81	0.07
CESM	15750	0.71	0.18	0.84	0.07
CSIRO	15750	0.70	0.18	0.80	0.06
F-GOALS	19000	0.72	0.18	0.77	0.08
HadCM3	13375	0.70	0.18	0.82	0.06
IPSL	6750	0.70	0.18	0.80	0.07
MIROC	11125	0.71	0.18	0.84	0.07
MPI	10250	0.70	0.18	0.80	0.07
MRI	20250	0.71	0.17	0.78	0.06

## LIST OF FIGURES

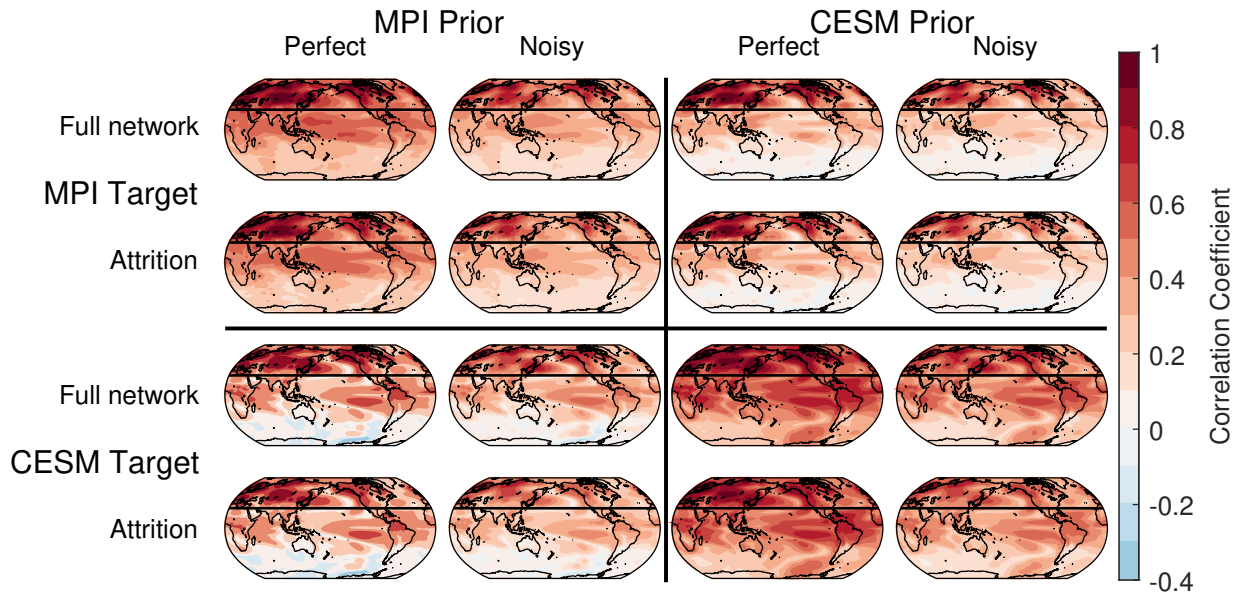
1009		
1010	<b>Fig. 1.</b>	Locations of the 54 NTREND sites (Wilson et al. 2016). NTREND records were developed using ring-width data (TRW; circles), maximum latewood density (MXD; squares), or a mix of TRW, MXD, and blue intensity (Mixed; triangles). Marker color denotes the century in which each record begins. . . . . 55
1011		
1012		
1013		
1014	<b>Fig. 2.</b>	Local Pearson’s correlation coefficients of pseudo-proxy reconstruction temperature anomalies with the target fields. Correlation coefficients are calculated over the period 850-1988 CE. Major rows indicate the model used to generate the target field, and major columns show the model used to build the initial ensemble for each assimilation. Minor rows designate whether the proxy network exhibits no time attrition or realistic time attrition. Minor columns indicate whether reconstructions use perfect or noisy proxies. The top-left and bottom-right quadrants display the perfect-model experiments, while the top-right and bottom-left quadrants show the biased-model cases. The black line in each map indicates 30°N. . . . . 56
1015		
1016		
1017		
1018		
1019		
1020		
1021		
1022	<b>Fig. 3.</b>	Pseudo-proxy reconstruction skill for DA (left column), PPR (middle), and a comparison of the two (right). Skill metrics are relative to a CESM target field using noisy proxies and realistic temporal attrition. DA results are for a biased-model MPI prior. All skill metrics are computed over the period 850-1988 CE. In order the rows detail local Pearson’s correlation coefficients, RMSE values, temporal standard deviation ( $\sigma$ ) ratios, and mean biases. Comparison plots show DA skill minus PPR skill. The comparison plot of $\sigma$ ratios only considers grid points where $\sigma$ is underestimated in both the DA and PPR reconstruction. . . . . 57
1023		
1024		
1025		
1026		
1027		
1028		
1029	<b>Fig. 4.</b>	Extratropical MJJA time series for the multi-model mean reconstruction (blue), Berkeley Earth instrumental records (yellow), and Anchukaitis et al. (2017) (red). We provide two different measures of uncertainty for the DA time series: the average of the $2\sigma$ posterior ensemble width taken over the 10 reconstruction (light grey), and the $2\sigma$ width of variability arising from prior model selection (dark grey). Reconstructed temperature anomalies are shown in Celsius for the instrumental era (top), and full reconstruction (middle). A three year moving average has been applied to the time series in the middle panel. The bottom panel displays the 31-year, running standard deviation of the DA ensemble-mean and Anchukaitis et al. (2017) time series. . . . . 58
1030		
1031		
1032		
1033		
1034		
1035		
1036		
1037		
1038	<b>Fig. 5.</b>	Spatial skill metrics for the multi-model mean reconstruction. Maps detail Pearson correlation coefficients (top left), RMSE values (top right), $\sigma$ ratios (bottom left), and mean biases (bottom right) of reconstructed grid point time series relative to the Berkeley Earth instrumental dataset over the period 1901-1988 CE. White markers show the proxy network and marker symbols follow the convention in Figure 1. . . . . 59
1039		
1040		
1041		
1042		
1043	<b>Fig. 6.</b>	Reconstructed temperature anomalies (in Celsius) between the MCA (950-1250 CE) and LIA (1450-1850 CE) for the DA reconstructions. Each map shows the results for a particular model prior. . . . . 60
1044		
1045		
1046	<b>Fig. 7.</b>	As in 6, but for the temperature CFRs summarized in Table 3. . . . . 61
1047	<b>Fig. 8.</b>	Composite mean maps of the reconstructed temperature response in years containing a major tropical volcanic event. Events (N=20) are selected as tropical eruptions with a global forcing magnitude equal or larger than the 1884 Krakatoa eruption: this set consists of 916, 1108, 1171, 1191, 1230, 1258, 1276, 1286, 1345, 1453, 1458, 1595, 1601, 1641, 1695, 1809, 1815, 1832, 1836, and 1884 CE (Sigl et al. 2015; Anchukaitis et al. 2017). Temperature anomalies (in Celsius) are determined relative to the mean temperature of the five years preceding each volcanic event. Each map shows the results for a particular model prior. . . . . 62
1048		
1049		
1050		
1051		
1052		
1053		

1054 **Fig. 9.** As in Figure 8, but for the temperature CFRs summarized in Table 3 (rows). We only show  
1055 grid points with reconstructed values for at least 6 eruptions. Maps show the composite  
1056 mean response in years with a major tropical eruption (left), and in the year following a  
1057 major eruption (right). . . . . 63

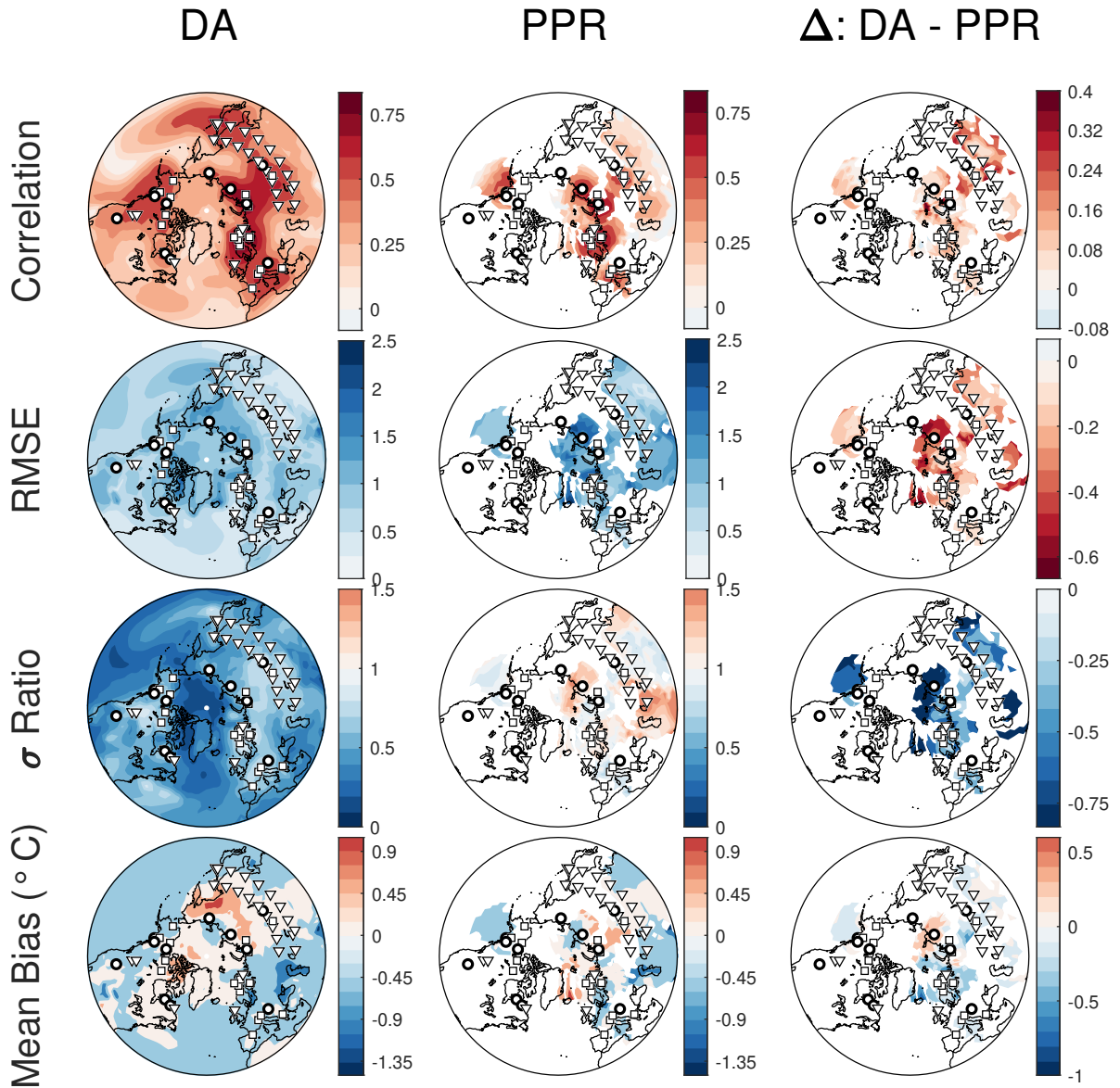
1058 **Fig. 10.** Spatial characteristics in the year following volcanic eruptions in 1257 (top) and 1600  
1059 (bottom) (De Silva and Zielinski 1998; Lavigne et al. 2013) in the multi-model mean recon-  
1060 struction. The left column displays temperature anomalies relative to the five preceding years  
1061 in Celsius. The middle column shows the average  $2\sigma$  width of the 10 posterior ensembles,  
1062 and the right column shows the  $2\sigma$  width of the multi-model ensemble. White markers show  
1063 the proxy network for each event. Marker symbols follow the convention in Figure 1. . . . . 64



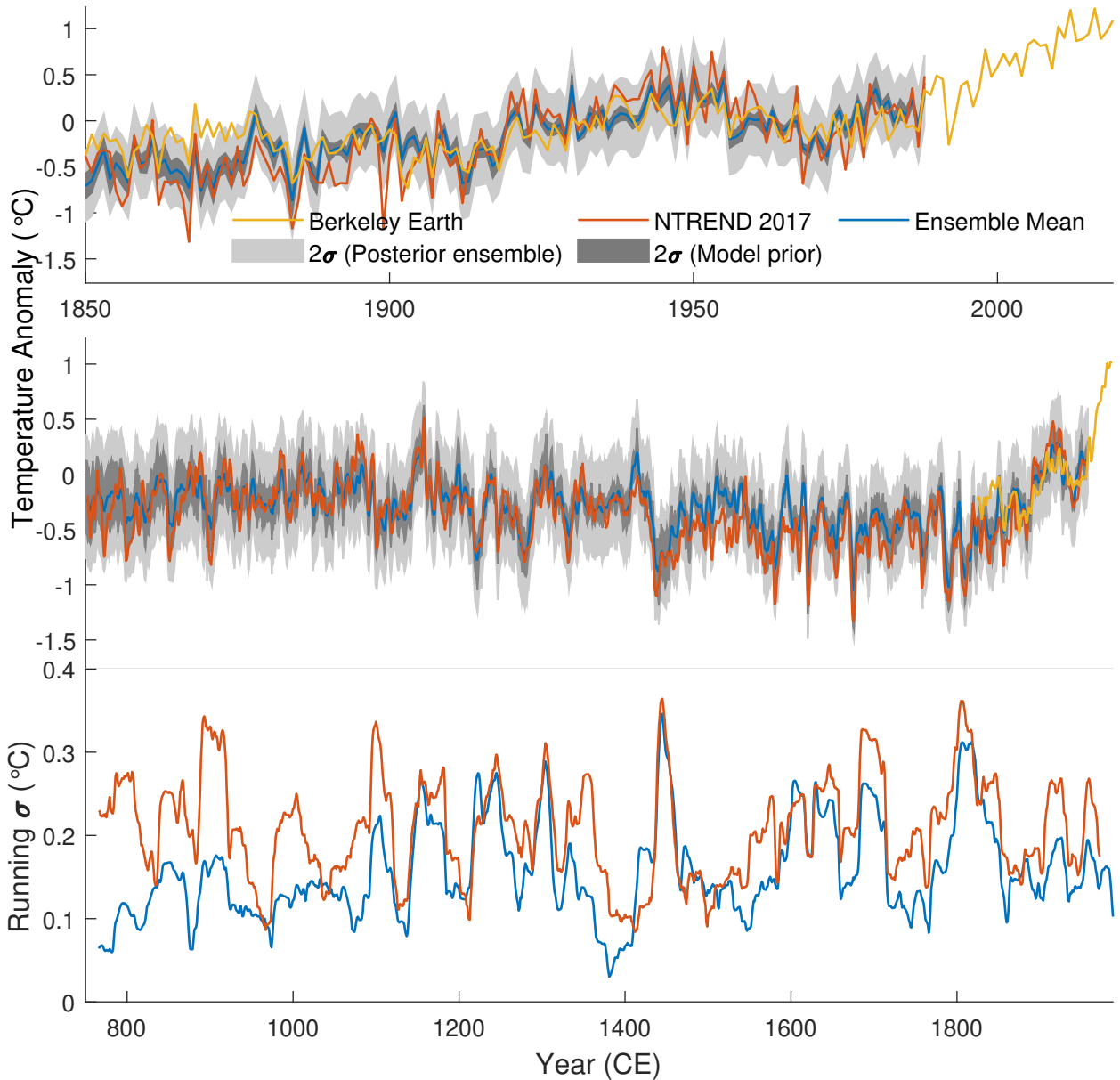
1064 FIG. 1. Locations of the 54 NTREND sites (Wilson et al. 2016). NTREND records were developed using  
 1065 ring-width data (TRW; circles), maximum latewood density (MXD; squares), or a mix of TRW, MXD, and blue  
 1066 intensity (Mixed; triangles). Marker color denotes the century in which each record begins.



1067 FIG. 2. Local Pearson's correlation coefficients of pseudo-proxy reconstruction temperature anomalies with  
 1068 the target fields. Correlation coefficients are calculated over the period 850-1988 CE. Major rows indicate the  
 1069 model used to generate the target field, and major columns show the model used to build the initial ensemble  
 1070 for each assimilation. Minor rows designate whether the proxy network exhibits no time attrition or realistic  
 1071 time attrition. Minor columns indicate whether reconstructions use perfect or noisy proxies. The top-left and  
 1072 bottom-right quadrants display the perfect-model experiments, while the top-right and bottom-left quadrants  
 1073 show the biased-model cases. The black line in each map indicates 30°N.

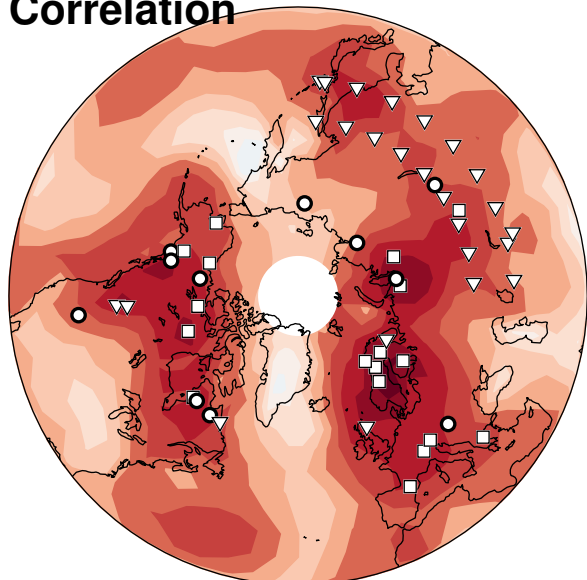


1074 FIG. 3. Pseudo-proxy reconstruction skill for DA (left column), PPR (middle), and a comparison of the two  
 1075 (right). Skill metrics are relative to a CESM target field using noisy proxies and realistic temporal attrition. DA  
 1076 results are for a biased-model MPI prior. All skill metrics are computed over the period 850-1988 CE. In order  
 1077 the rows detail local Pearson's correlation coefficients, RMSE values, temporal standard deviation ( $\sigma$ ) ratios, and  
 1078 mean biases. Comparison plots show DA skill minus PPR skill. The comparison plot of  $\sigma$  ratios only considers  
 1079 grid points where  $\sigma$  is underestimated in both the DA and PPR reconstruction.

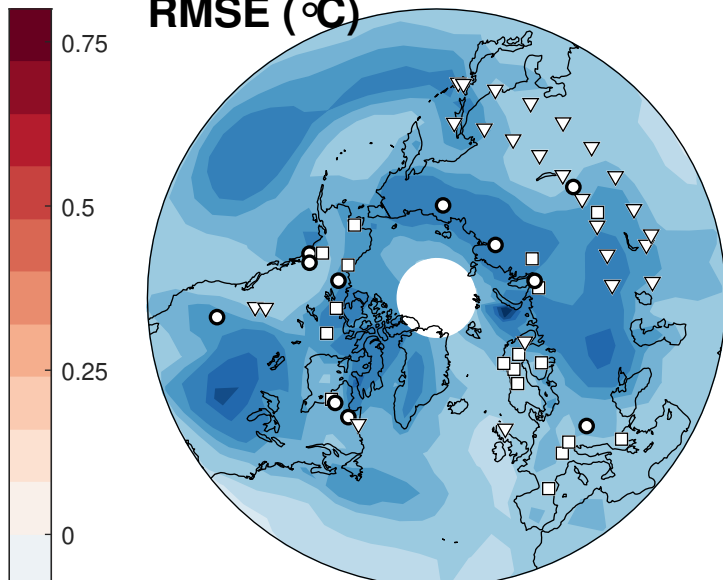


1080 FIG. 4. Extratropical MJA time series for the multi-model mean reconstruction (blue), Berkeley Earth  
 1081 instrumental records (yellow), and Anchukaitis et al. (2017) (red). We provide two different measures of  
 1082 uncertainty for the DA time series: the average of the  $2\sigma$  posterior ensemble width taken over the 10 reconstruction  
 1083 (light grey), and the  $2\sigma$  width of variability arising from prior model selection (dark grey). Reconstructed  
 1084 temperature anomalies are shown in Celsius for the instrumental era (top), and full reconstruction (middle). A  
 1085 three year moving average has been applied to the time series in the middle panel. The bottom panel displays the  
 1086 31-year, running standard deviation of the DA ensemble-mean and Anchukaitis et al. (2017) time series.

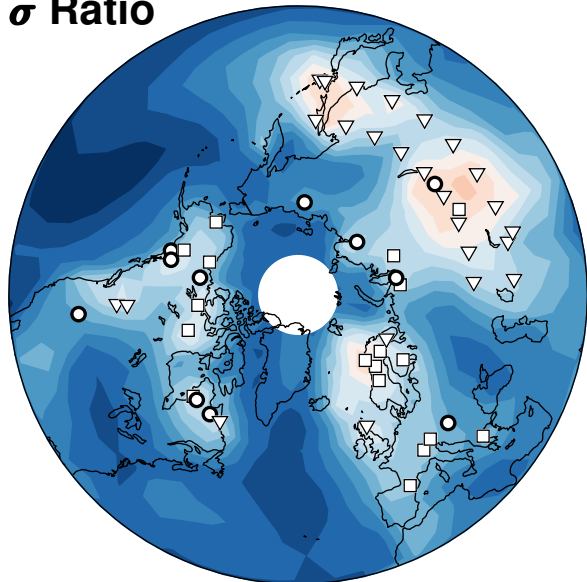
### Correlation



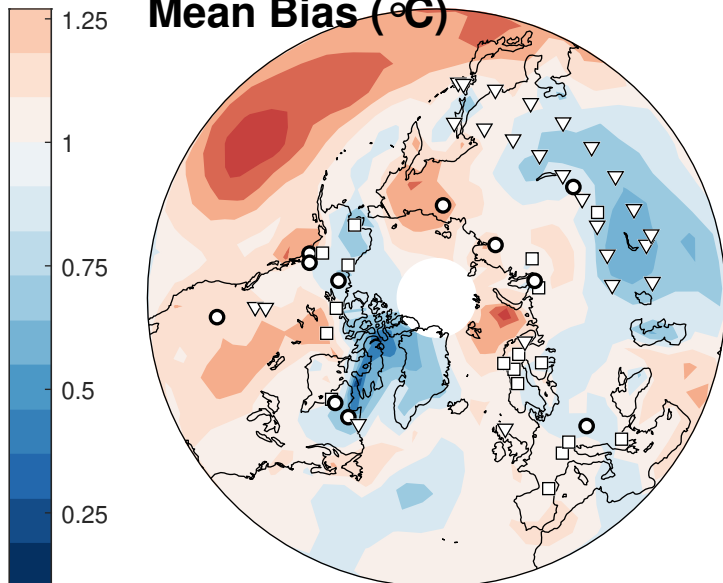
### RMSE ( $^{\circ}\text{C}$ )



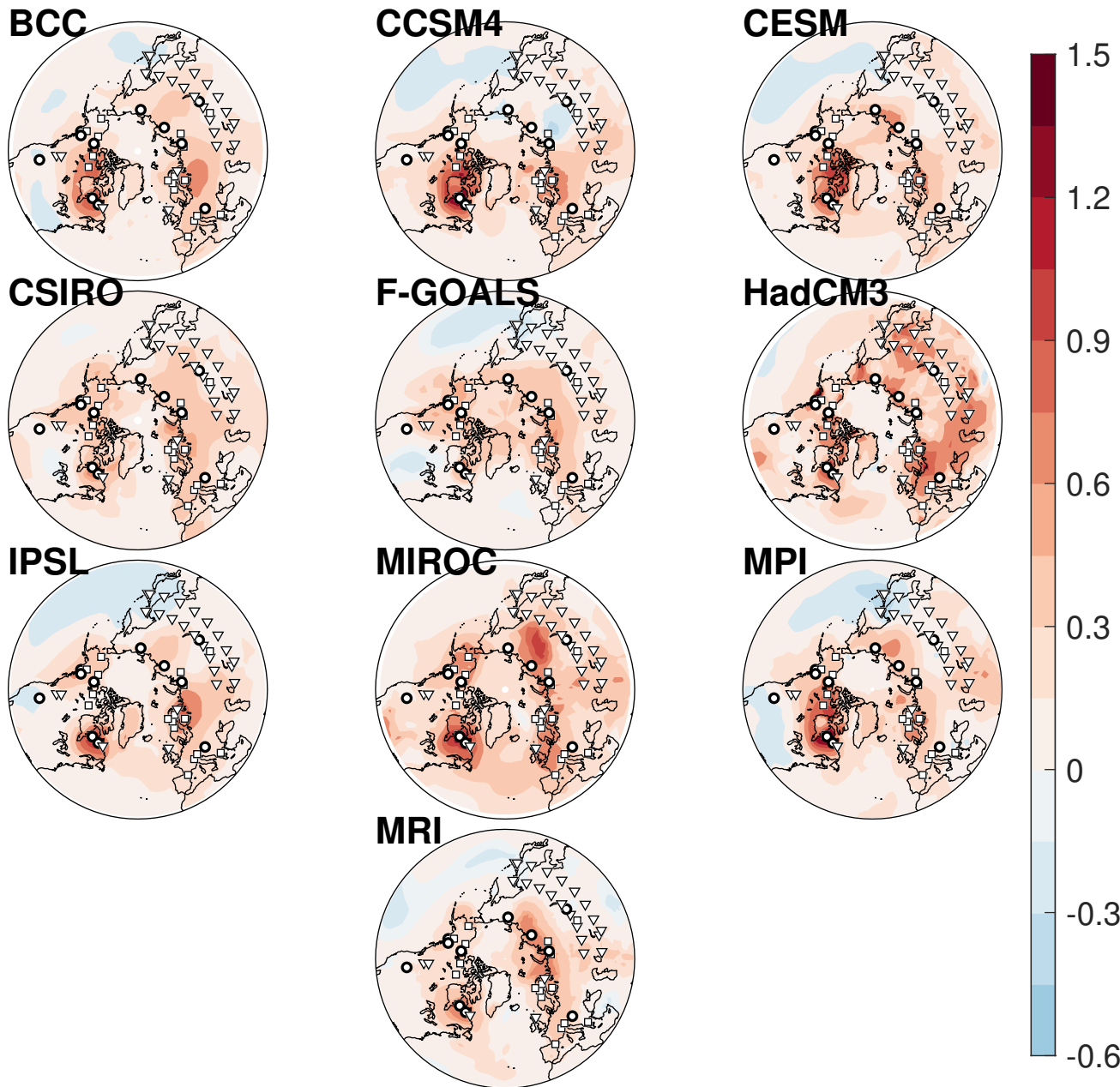
### $\sigma$ Ratio



### Mean Bias ( $^{\circ}\text{C}$ )



1087 FIG. 5. Spatial skill metrics for the multi-model mean reconstruction. Maps detail Pearson correlation  
1088 coefficients (top left), RMSE values (top right),  $\sigma$  ratios (bottom left), and mean biases (bottom right) of  
1089 reconstructed grid point time series relative to the Berkeley Earth instrumental dataset over the period 1901-1988  
1090 CE. White markers show the proxy network and marker symbols follow the convention in Figure 1.



1091 FIG. 6. Reconstructed temperature anomalies (in Celsius) between the MCA (950-1250 CE) and LIA (1450-  
 1092 1850 CE) for the DA reconstructions. Each map shows the results for a particular model prior.

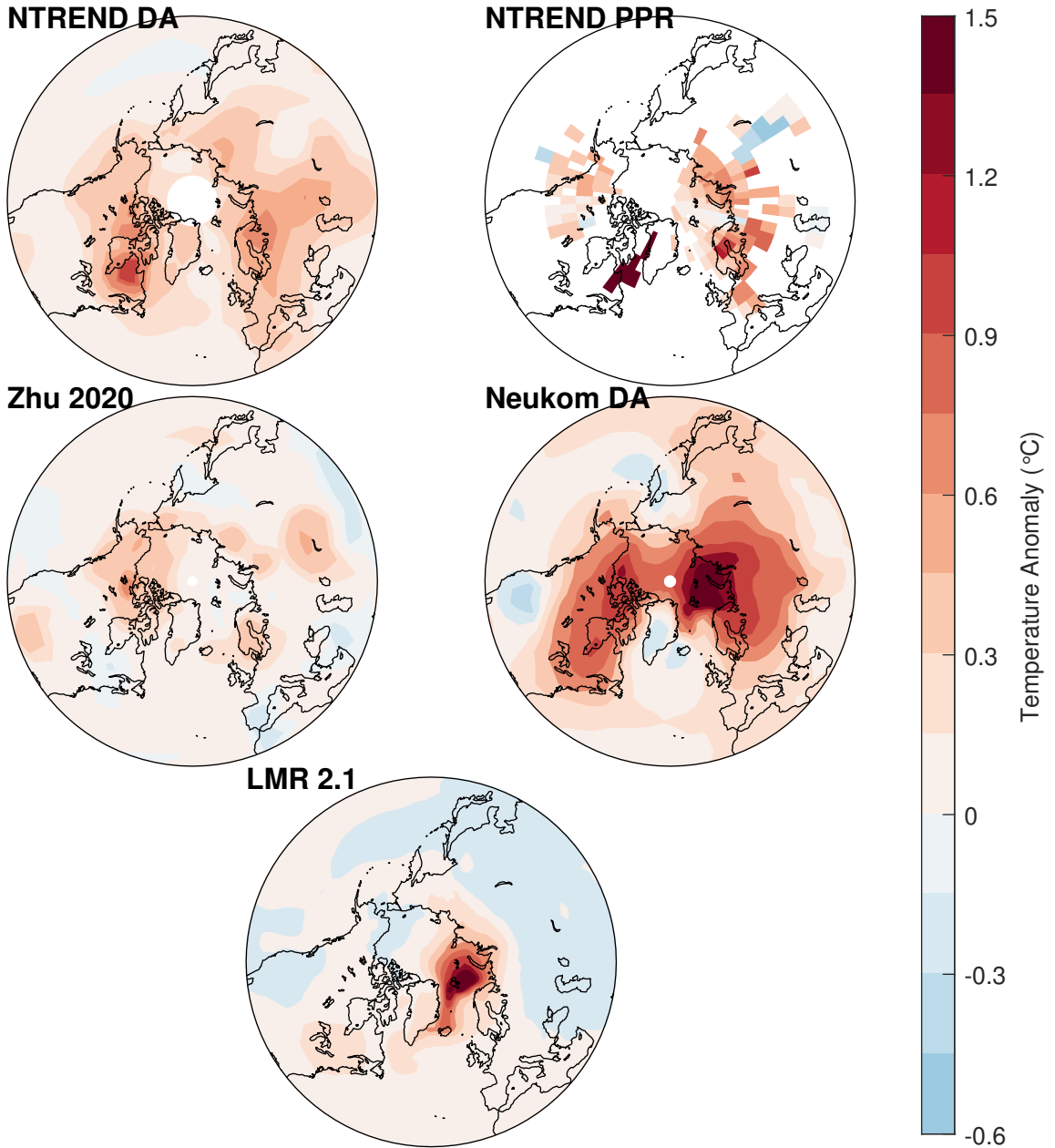
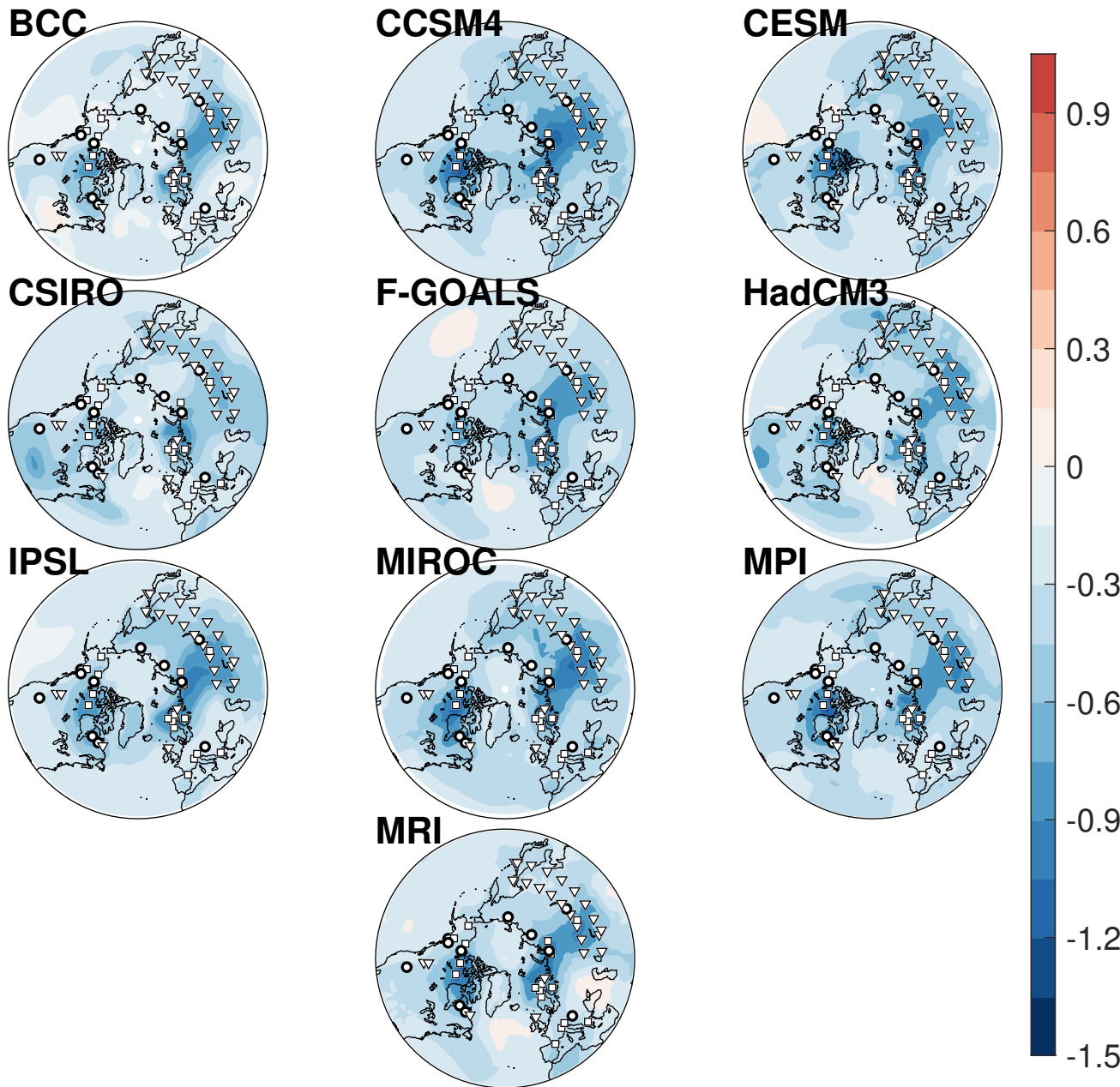
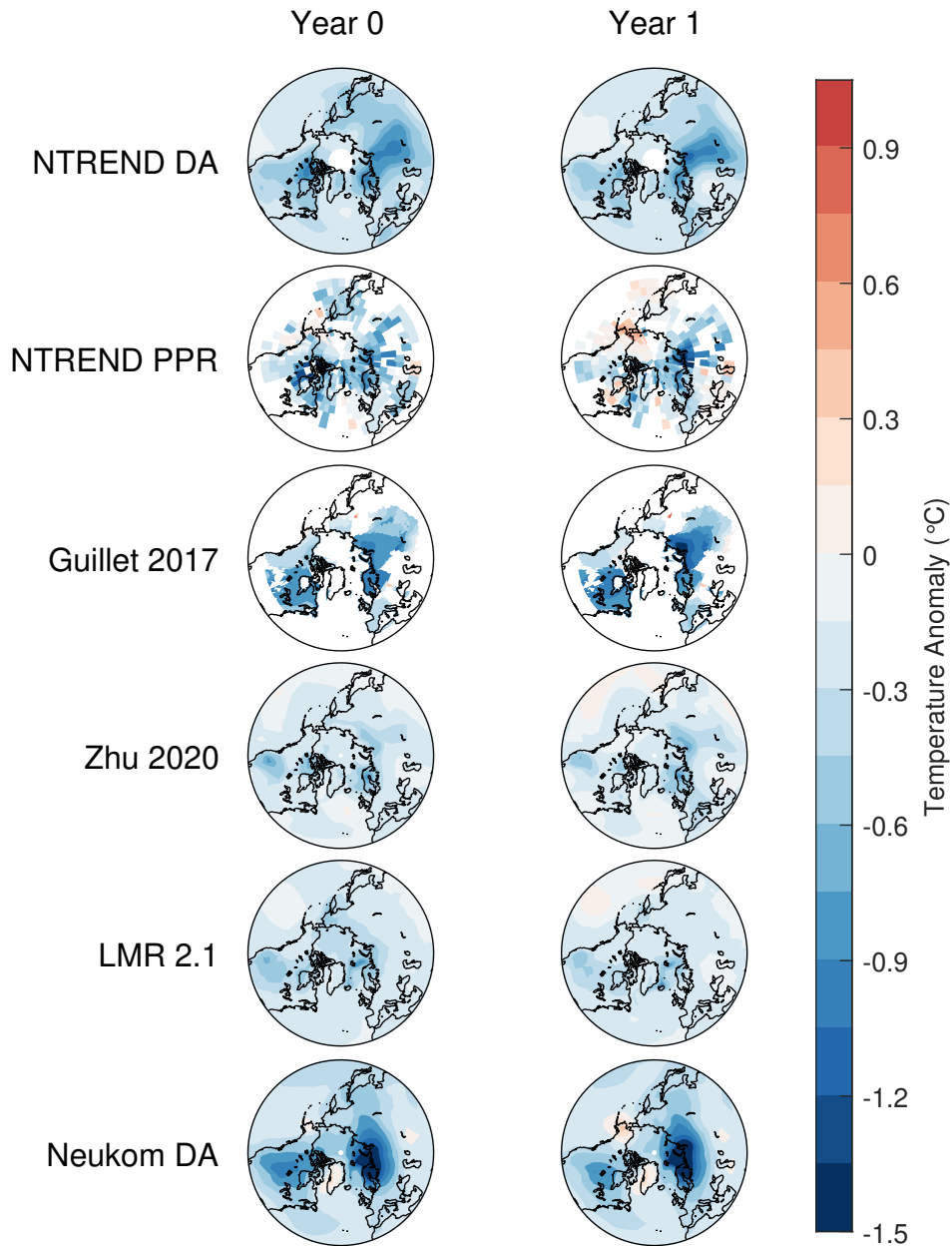


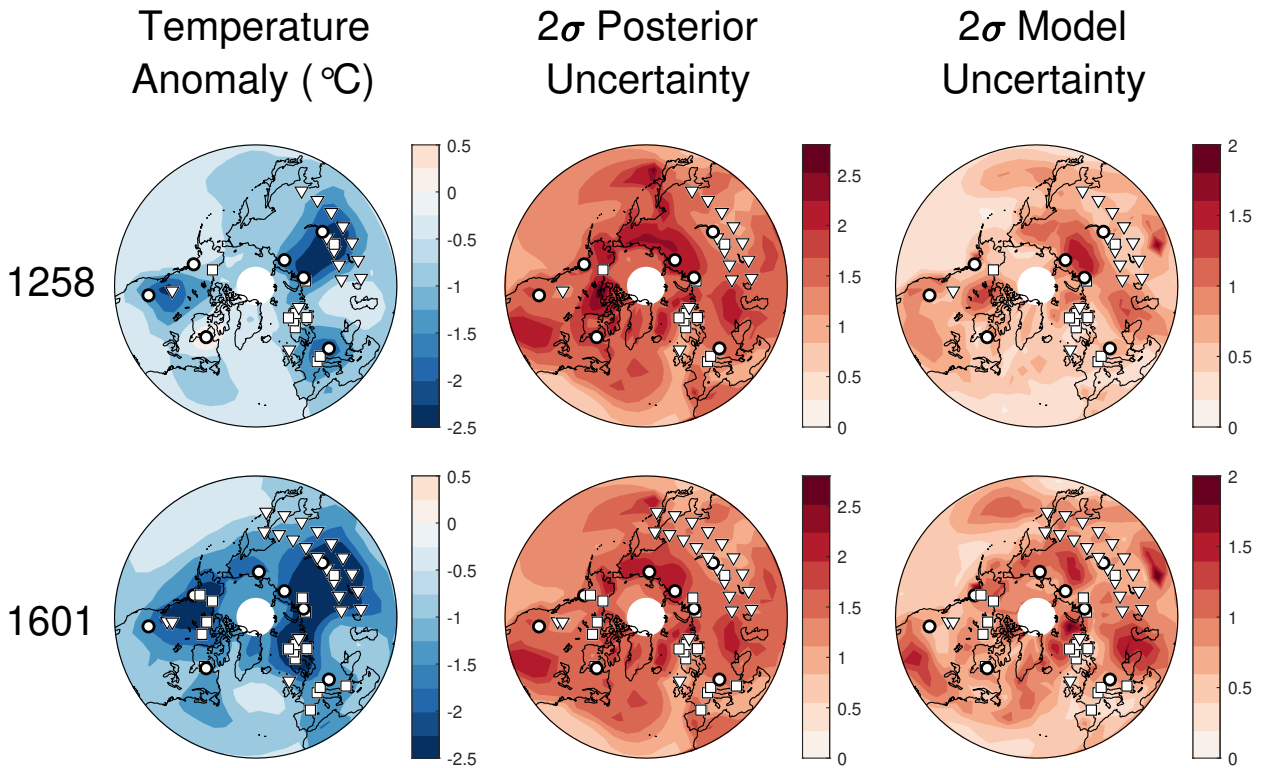
FIG. 7. As in 6, but for the temperature CFRs summarized in Table 3.



1093 FIG. 8. Composite mean maps of the reconstructed temperature response in years containing a major tropical  
 1094 volcanic event. Events (N=20) are selected as tropical eruptions with a global forcing magnitude equal or larger  
 1095 than the 1884 Krakatoa eruption: this set consists of 916, 1108, 1171, 1191, 1230, 1258, 1276, 1286, 1345,  
 1096 1453, 1458, 1595, 1601, 1641, 1695, 1809, 1815, 1832, 1836, and 1884 CE (Sigl et al. 2015; Anchukaitis et al.  
 1097 2017). Temperature anomalies (in Celsius) are determined relative to the mean temperature of the five years  
 1098 preceding each volcanic event. Each map shows the results for a particular model prior.



1099 FIG. 9. As in Figure 8, but for the temperature CFRs summarized in Table 3 (rows). We only show grid points  
 1100 with reconstructed values for at least 6 eruptions. Maps show the composite mean response in years with a major  
 1101 tropical eruption (left), and in the year following a major eruption (right).



1102 FIG. 10. Spatial characteristics in the year following volcanic eruptions in 1257 (top) and 1600 (bottom)  
 1103 (De Silva and Zielinski 1998; Lavigne et al. 2013) in the multi-model mean reconstruction. The left column  
 1104 displays temperature anomalies relative to the five preceding years in Celsius. The middle column shows the  
 1105 average  $2\sigma$  width of the 10 posterior ensembles, and the right column shows the  $2\sigma$  width of the multi-model  
 1106 ensemble. White markers show the proxy network for each event. Marker symbols follow the convention in  
 1107 Figure 1.



18 **LIST OF TABLES**

19 **Table S1.** Pseudo-proxy localization radii and split-sample validation metrics. As in Table  
20 2, but using climate model output as the target field. . . . . 3

21 **Table S2.** Skill metrics for pseudo-proxy reconstructions of mean extratropical May-  
22 August time series. DA reconstructions use the realistic biased-model, noisy-  
23 proxy, time-attrition experimental design. PPR time series and target time series  
24 are calculated using only the grid cells for which RE>0 in each reconstructed  
25 time step. . . . . 4

26 TABLE S1. Pseudo-proxy localization radii and split-sample validation metrics. As in Table 2, but using  
 27 climate model output as the target field.

Target	Prior	Localization Radius (km)	Correlation	RMSE (°C)	$\sigma$ Ratio	Mean Bias (°C)
CESM	CESM	$\infty$	0.73	0.18	0.76	0.02
CESM	MPI	$\infty$	0.72	0.19	0.91	0.02
MPI	CESM	$\infty$	0.74	0.21	0.62	0.09
MPI	MPI	$\infty$	0.75	0.20	0.75	0.07

28 TABLE S2. Skill metrics for pseudo-proxy reconstructions of mean extratropical May-August time series. DA  
 29 reconstructions use the realistic biased-model, noisy-proxy, time-attrition experimental design. PPR time series  
 30 and target time series are calculated using only the grid cells for which RE>0 in each reconstructed time step.

Target Field	Reconstruction Method	Correlation	RMSE (°C)	$\sigma$ Ratio	Mean Bias (°C)
CESM	DA, MPI Prior	0.67	0.20	0.84	-0.03
	PPR	0.68	0.25	0.96	0.03
MPI	DA, CESM Prior	0.74	0.41	0.66	0.35
	PPR	0.73	0.46	0.84	0.37

31 **LIST OF FIGURES**

32 **Fig. S1.** As in Figure 2, but for RMSE ( $^{\circ}\text{C}$ ). . . . . 6

33 **Fig. S2.** As in Figure 2, but for  $\sigma$  ratios. . . . . 7

34 **Fig. S3.** As in Figure 2, but for mean biases ( $^{\circ}\text{C}$ ). . . . . 8

35 **Fig. S4.** Extratropical MJJA time series for the pseudo-proxy experiments with a CESM target.  
36 Reconstructed temperature anomalies are shown in Celsius (top) for the DA reconstruction  
37 (blue) and PPR reconstruction (red) along with the reconstruction target (yellow). The  
38 bottom panel displays a 31 year running standard deviation for each time series. A three year  
39 moving average has been applied to all time series. . . . . 9

40 **Fig. S5.** As in Supplemental Figure 4, but for an MPI target. . . . . 10

41 **Fig. S6.** As in Figure 3, but for a MPI target field. Here, the DA reconstructions use a CESM prior. . . . 11

42 **Fig. S7.** Extratropical MJJA time series for the individual DA reconstructions. Each time series shows  
43 the results for a particular model prior. A 31 year moving average has been applied to each  
44 time series. . . . . 12

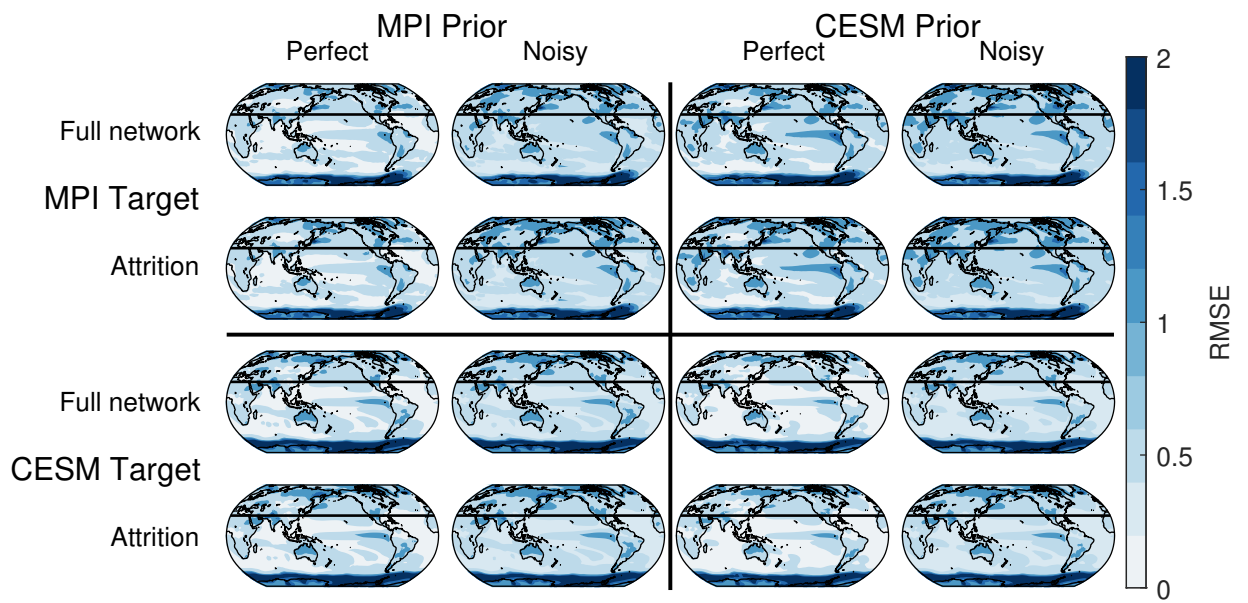


FIG. S1. As in Figure 2, but for RMSE (°C).

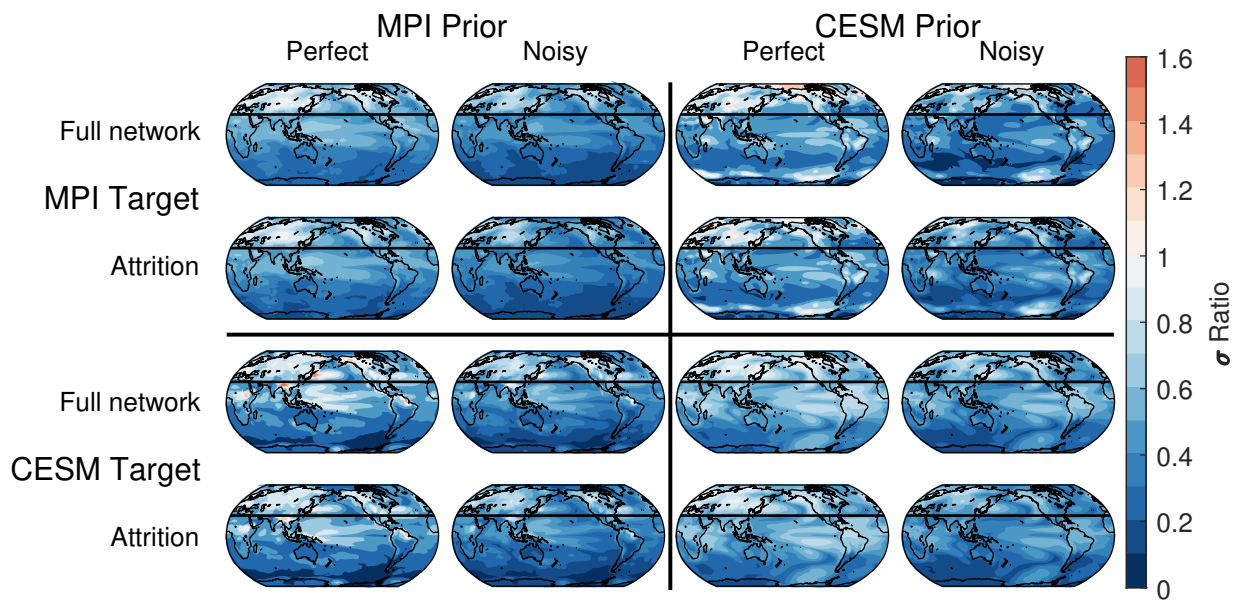


FIG. S2. As in Figure 2, but for  $\sigma$  ratios.

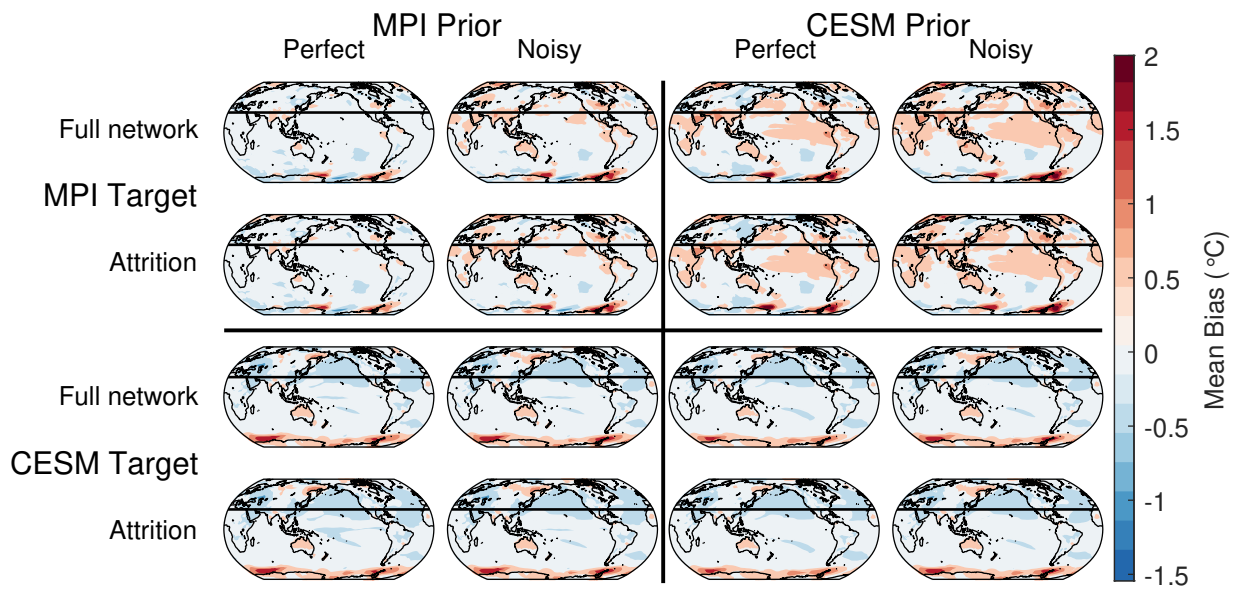
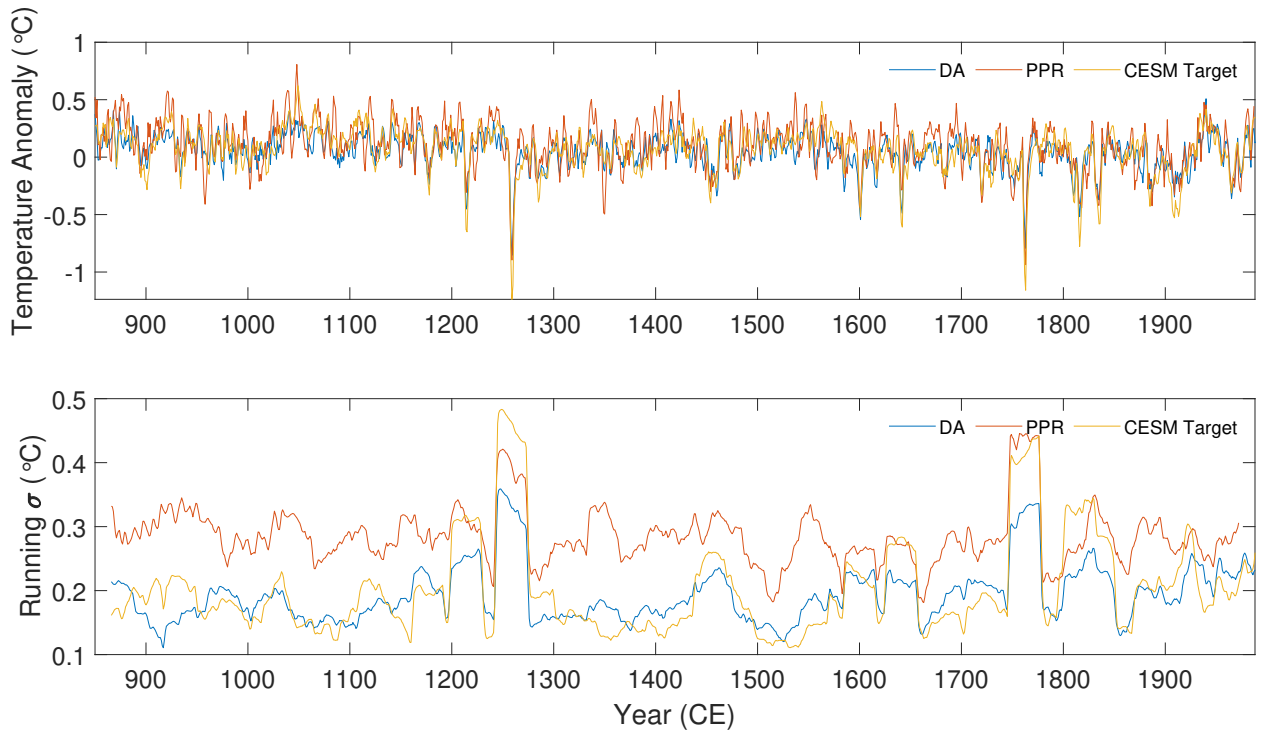


FIG. S3. As in Figure 2, but for mean biases (°C).



45 FIG. S4. Extratropical MJJA time series for the pseudo-proxy experiments with a CESM target. Reconstructed  
 46 temperature anomalies are shown in Celsius (top) for the DA reconstruction (blue) and PPR reconstruction (red)  
 47 along with the reconstruction target (yellow). The bottom panel displays a 31 year running standard deviation  
 48 for each time series. A three year moving average has been applied to all time series.

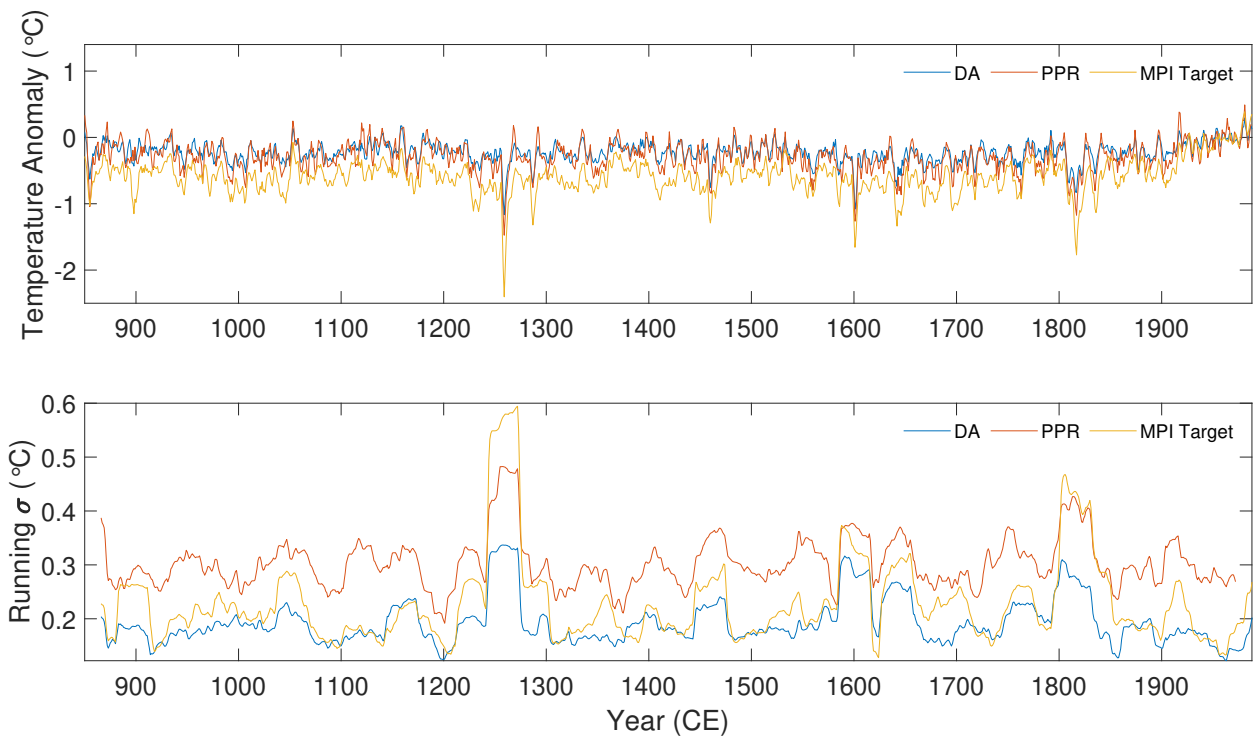


FIG. S5. As in Supplemental Figure 4, but for an MPI target.

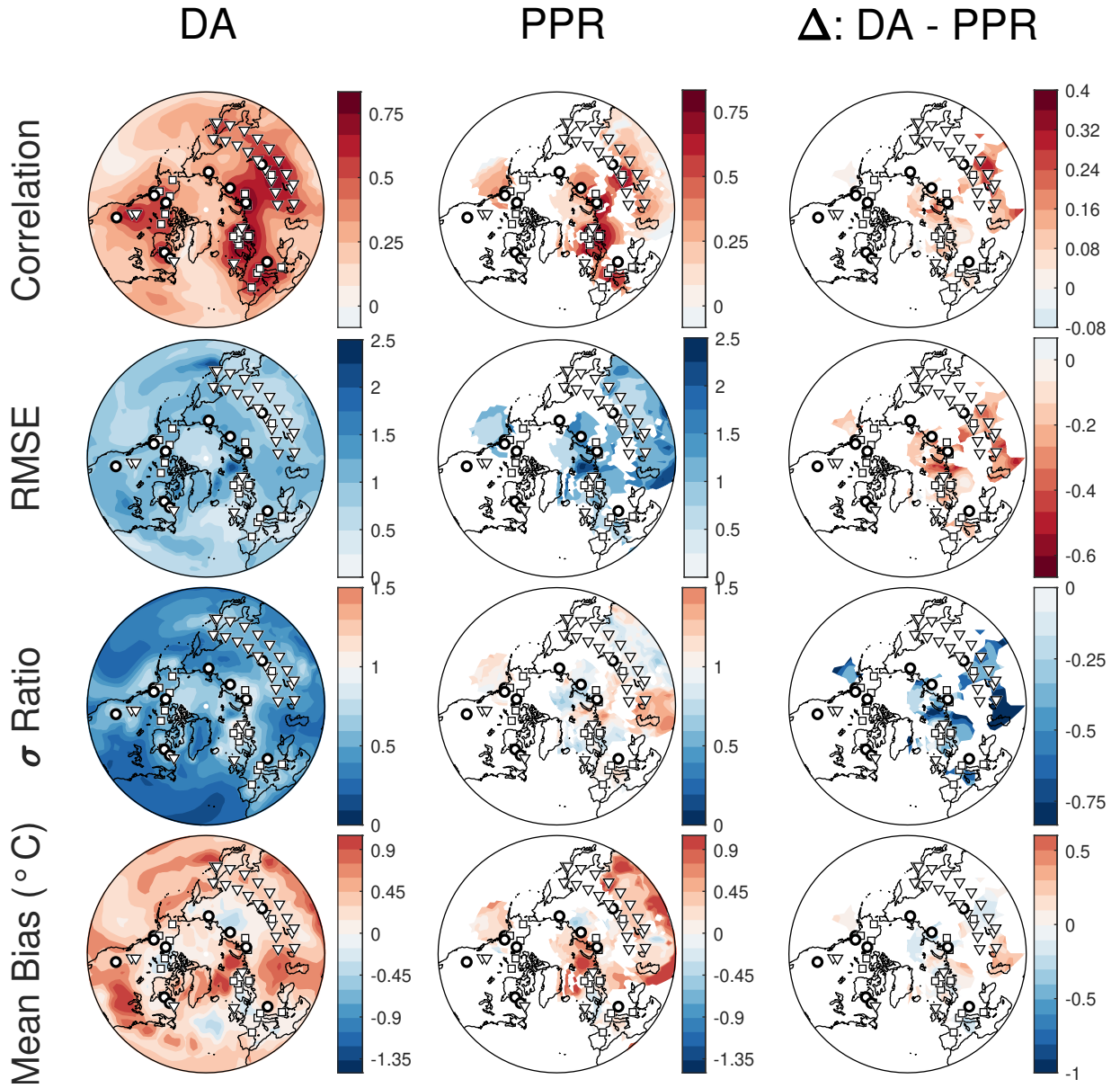
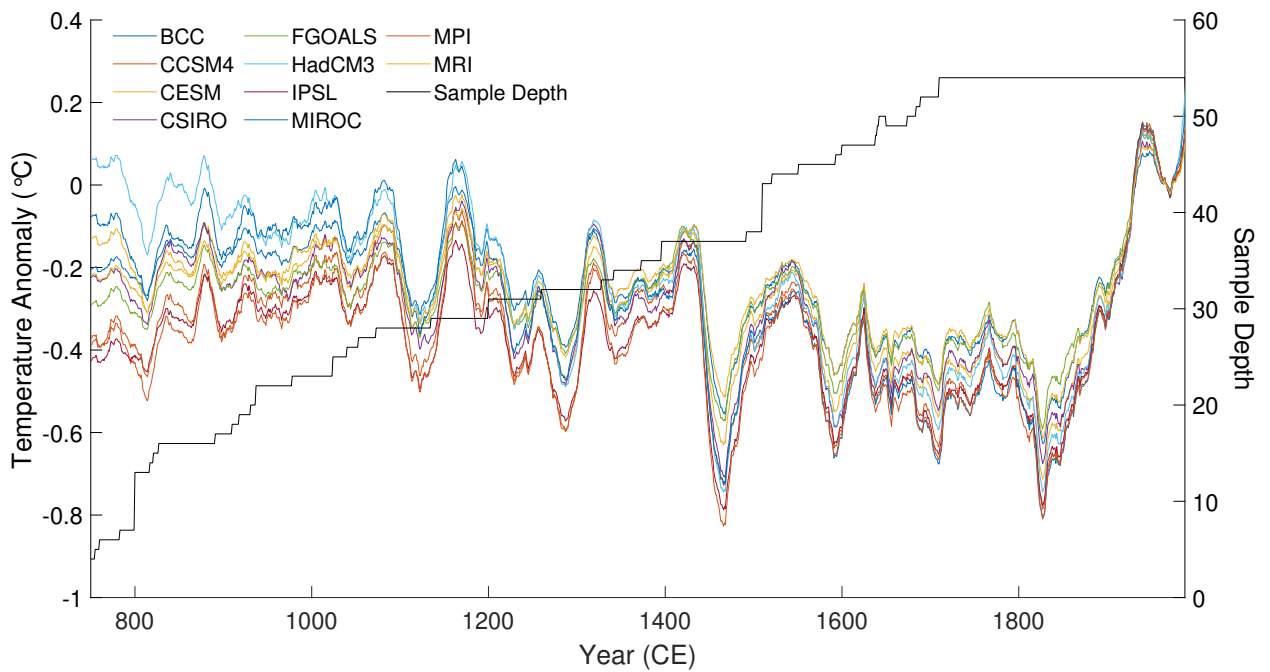


FIG. S6. As in Figure 3, but for a MPI target field. Here, the DA reconstructions use a CESM prior.



49 FIG. S7. Extratropical MJA time series for the individual DA reconstructions. Each time series shows the  
 50 results for a particular model prior. A 31 year moving average has been applied to each time series.